The Astrophysical Journal, 681:1557–1573, 2008 July 10

EFFECTS OF METALLICITY ON THE CHEMICAL COMPOSITION OF CARBON STARS

J. M. Leisenring,[1] F. Kemper,[2,1] and G. C. Sloan[3]

Received 2007 December 4; accepted 2008 March 17

ABSTRACT

We present *Spitzer* IRS data on 19 asymptotic giant branch (AGB) stars in the Large Magellanic Cloud, complementing existing published data sets of carbon stars in both Magellanic Clouds and the Milky Way, to investigate the effects of metallicity on dust and molecular spectral features arising from the circumstellar envelope. We find that the C_2H_2 *P*- and *R*-branches at 7.5 μm are affected by dust dilution at higher mass-loss rates—albeit to a lesser extent for sources in the Magellanic Clouds, compared to the Milky Way—while the narrow 13.7 μm C_2H_2 *Q*-branch only shows the effect of dust dilution at low mass-loss rates. A strong metallicity dependence is not observed for the *Q*-branch. Independent of metallicity, we also provide an explanation for the observed shifts in the central wavelength of the SiC emission feature, as we show that these are largely caused by molecular band absorption on either side of the dust emission feature, dominating over shifts in the central wavelength caused by self-absorption. We have devised a method to study the dust condensation history in carbon-rich AGB stars in different metallicity environments, by measuring the strength of the 11.3 μm SiC and 30 μm MgS features with respect to the continuum, as a function of mass-loss rate. With this method, it is possible to distinguish in what order SiC and graphite condense, which is believed to be sensitive to the metallicity, prior to the eventual deposit of the MgS layer.

Subject headings: circumstellar matter — infrared: stars — Magellanic Clouds — stars: AGB and post-AGB — stars: carbon — stars: mass loss

Online material: color figures

1. INTRODUCTION

Stars with a main-sequence mass of $\sim$1–8 $M_\odot$ undergo an asymptotic giant branch (AGB) phase which plays an important role in the recycling of stellar material into the ISM. During the AGB phase, a significant fraction (up to 90%; Weidemann 1987) of the stellar mass is lost in a gradual stellar wind. Initially, this wind results in a mass-loss rate of $10^{-7}\ M_\odot\ \mathrm{yr}^{-1}$ and eventually evolves toward a superwind phase with $\dot{M} \sim 10^{-4}\ M_\odot\ \mathrm{yr}^{-1}$ (Habing 1996). Given the shape of the initial mass function, AGB stars contribute a substantial amount of gas and dust to the ISM (about half the total recycled gas material), driving further galactic evolution (Maeder 1992).

The mass-loss mechanisms still remain poorly understood, even though efforts at modeling are decades old (Salpeter 1974). Thermal pulses enrich the star's outer layers by extending a convective zone downward to the He shell and allowing carbon to be mixed to the surface (Schwarzschild & Härm 1965; Herwig et al. 2007). Material then flows from the stellar surface due to an unknown mass-loss mechanism. Once the gas has cooled enough to allow the formation of molecules and condensation of dust grains, the impeding radiation pressure from the central source on these grains is sufficient to accelerate the grains and drive a dust-driven wind by grain-gas drag (Hoyle & Wickramasinghe 1962; Fleischer et al. 1995; Höfner et al. 1995). The complex interplay between the internal thermal pulses, the dust-driven wind, and envelope pulsations provides the theoretical framework for the observed light curves and mass-loss rates (Whitelock et al. 1997).

The efficiency of grain formation and rate of grain growth is thus expected to affect the mass-loss history of AGB stars. We can constrain dust formation within the circumstellar envelopes of AGB stars by analyzing the isotopic compositions of certain grains found in primitive meteorites. Since these meteorite compositions are found to differ greatly from solar compositions, they must have originated prior to the formation of our solar system and are thus dubbed "presolar." Detailed studies of presolar grain characteristics (such as sizes, crystal structures, and composition) can be accomplished after extraction from the meteorites (Bernatowicz & Zinner 1997; Nittler 2003; Clayton & Nittler 2004; Zinner et al. 2006). These dust grains are virtually unaltered from their formation state in AGB star and thus provide constraints on the physical characteristics of the dust we observe in the circumstellar shells of Galactic AGB stars. Silicon carbide (SiC) and carbon graphite dust grains account for the majority of discovered presolar grains and can be attributed to formation in Galactic carbon stars (Bernatowicz et al. 2006, p. 109). Due to the aggressive and destructive nature of analyzing the meteorites, all but the most refractory grains become dissolved. Only recently have presolar silicates been discovered meteorites and interplanetary dust particles (Messenger et al. 2005).

Initially, the mass loss occurs from the outer layers of the star, and hence the chemical composition of the recycled material reflects the original ISM composition from which the star was formed. As mass loss progresses, dredge-up processes enrich the stellar ejecta with nuclear fusion products (C, O), *s*-process elements (Ba, Pb), and lithium (Dray et al. 2003). The nuclear fusion produces more carbon than oxygen (Lattanzio et al. 2000), consequently causing the C/O ratio of the stellar atmosphere to increase from dredge-up of material produced in the H- and He-burning layers. For a solar-metallicity environment, Straniero et al. (1997) find that AGB stars above $\sim$1.5 $M_\odot$ will eventually become carbon stars unless they exhibit the hot bottom burning phenomenon of more massive stars ($M \gtrsim 5\ M_\odot\ \mathrm{yr}^{-1}$; Pols et al. 2001). However, those with a lower metallicity initially contain less oxygen in their atmospheres than their metal-rich cousins and,

[1] Astronomy Department, University of Virginia, Charlottesville, VA 22904.
[2] Jodrell Bank Centre for Astrophysics, University of Manchester, Manchester M13 9PL, UK.
[3] Astronomy Department, Cornell University, Ithaca, NY 14853.

therefore, will more easily become carbon stars. Thus, as metallicity decreases, the lower mass limit at which stars will evolve into carbon stars also decreases (Renzini & Voli 1981; Vassiliadis & Wood 1993). In addition, metallicity may have a profound effect on grain growth, the number density of grains, and the grain size distribution, thus altering the influence of the radiation pressure from the central star. The chemical composition of material in the wind will also be affected by the metallicity.

The Magellanic Clouds provide excellent laboratories to study the effects of metallicity on the formation of dust. Since the distances to these galaxies and their metallicities are well-known, we can derive absolute dust mass-loss rates from observed spectral energy distributions (Le Bertre 1997; Groenewegen et al. 2007). On average, the Large Magellanic Cloud's (LMC's) metallicity is about half that of the Sun, while the metallicity of the Small Magellanic Cloud (SMC) is approximately 0.2 compared to solar (Russell & Bessell 1989; Bertelli et al. 1994). While most Galactic AGB stars appear to show an oxygen-rich chemistry, the Magellanic Clouds contain a larger fraction of carbon stars, in line with their lower metallicities (Blanco et al. 1980).

Here we present data from the Infrared Spectrograph (IRS; Houck et al. 2004) aboard the *Spitzer Space Telescope* (Werner et al. 2004) on 19 carbon-rich AGB stars that we combine with previously published carbon star samples (Sloan et al. 2006; Zijlstra et al. 2006; Lagadec et al. 2007; hereafter collectively SZL). The combination of these large samples of Galactic, LMC, and SMC spectra provides us with a tool to analyze the effects of metallicity on the composition of the dust and gas and allows us to better understand the dust condensation sequence, the efficiency of grain formation, and ultimately the mass-loss rates.

2. OBSERVATIONS

2.1. *Sample Selection and Selection Effects*

We present *Spitzer* IRS data of 19 carbon-rich AGB stars in the LMC (Fig. 1, Table 1). Based on the color classification from Egan et al. (2001) these objects were originally observed for a survey of the dust condensation sequence in oxygen-rich AGB stars, but their IRS spectral signatures clearly identify them as being carbon rich. This sample covers the same range of $H - K_s$ vs. $K_s - A$ color-color space as those LMC objects published by Zijlstra et al. (2006), thereby nearly doubling the available data points. The IRS spectrum of IRAS 04496−6958 was previously published by Speck et al. (2006).

In order to analyze the effects of metallicity, we compare the combined LMC sample to C-rich AGB stars observed in the SMC and Milky Way. The SMC stars included here were observed using the IRS and presented in two separate papers by Sloan et al. (2006) and Lagadec et al. (2007). We used Galactic data observed with the *Infrared Space Observatory* (*ISO*) and published in the Short-Wavelength Spectrometer (SWS) Atlas (Sloan et al. 2003). Thus, we present carbon stars from three different metallicity environments: 29 objects residing in the SMC, 44 from the LMC, and 34 Galactic carbon stars.

The SWS instrument on *ISO* observed stars previously known to be carbon stars in the Milky Way with a wide range of colors. Since the threshold mass to form a carbon star is high in single-star evolution in the Galaxy, not all of these are "normal" AGB stars. In particular, the blue stars are more peculiar high-mass stars or binaries (Olson & Richer 1975). Whereas more than half of the Galactic sample contains blue objects expected to be naked carbon stars, the LMC and SMC samples are much redder on average. This is a known selection effect, since the Magellanic Cloud surveys were selected from the mid-IR color classification scheme using 2MASS and *MSX* colors (Egan et al. 2001). Since *MSX* is only sensitive toward objects with a strong 8 μm excess, it was expected that most of the observed objects would have high mass-loss rates and relatively red spectra. Indeed, for most of the Magellanic Cloud objects we find gas mass-loss rates of $10^{-6}\ M_\odot\ \mathrm{yr}^{-1}$ or higher, while Galactic AGB stars have a wider range of $10^{-8.5}$ to $10^{-4.5}\ M_\odot\ \mathrm{yr}^{-1}$ (§ 3.3). The Galactic sample contains the widest range of colors, spanning the range $0.3 \lesssim H - K_s \lesssim 4.5$, while the LMC and SMC objects span the range $1 \lesssim H - K_s \lesssim 3.2$ and $0.9 \lesssim H - K_s \lesssim 2.1$, respectively. On average, the carbon stars observed in the LMC are redder than those observed in the SMC.

2.2. *Spectral Features*

2.2.1. C_2H_2 *Absorption*

For the majority of stars in the three samples, the most prominent molecular absorption features occur at ∼7.5 and ∼14 μm and are normally associated with acetylene (C_2H_2) absorption. However, HCN and CS absorption are also known to provide contributions to the depth of these features (Goebel et al. 1981; Aoki et al. 1998). Using the 3.5 μm absorption feature, van Loon et al. (2006) show that HCN and CS are comparatively weak for LMC stars, while Matsuura et al. (2006) found no clear evidence of HCN among their LMC sample. In particular, they interpret the low HCN abundance in the Magellanic Clouds as being due to initially low nitrogen abundances and efficient carbon production in metal-poor environments. Aoki et al. (1999) and Cernicharo et al. (1999) only detect HCN in 1/3 of their Galactic carbon sample. Thus, we can confidently identify these two absorptions as prominently due to C_2H_2.

The double-peaked absorption band centered at 7.5 μm arises from the C_2H_2 $\nu_4^1 + \nu_5^1$ transitions in the *P*- and *R*-branches. The *Q*-branch band of the C_2H_2 fundamental ν_5 bending mode creates a sharp absorption feature at 13.7 μm. Colder gas in the extended envelope (possibly above the dust-forming region) produces the sharp *Q*-branch feature while the broad *P*- and *R*-branches originate from warmer gas deeper into the atmosphere (Jørgensen et al. 2000). Matsuura et al. (2006) explain the broad wings extending on either side of the 13.7 μm feature as being due to the *P*- and *R*-branches. In the most extreme cases, these wings can extend between ∼11 and ∼17 μm (Speck et al. 2006). Throughout this paper, we refer to the *Q*-branch as the "13.7 μm feature" and the *P*- and *R*-branches in the same region as the "14 μm feature."

2.2.2. 10 μm *Absorption*

A significant number of stars exhibit a relatively weak absorption band spanning ∼8.5 to ∼11 μm with a peak depth around 9.4 μm. We mainly observe this feature in the bluest objects. While the carrier of this feature is still in doubt, our observations support a molecule that originates near the photosphere of the star and would be masked by the infilling of dust emission in redder objects.

Jørgensen et al. (2000) and Zijlstra et al. (2006) favor an identification of C_3; however, we do not observe a corresponding absorption between 6.6 and 7 μm that is also predicted. Furthermore, we cannot use the deep absorption feature at 5 μm to confirm the presence of this molecule, since this band also contains significant contributions from CO. Laboratory measurements are necessary in order to firmly identify C_3 as the carrier of the 10 μm absorption.

2.2.3. SiC *Emission*

The majority of the carbon stars in the Magellanic Clouds and the Galaxy show the presence of an emission feature around

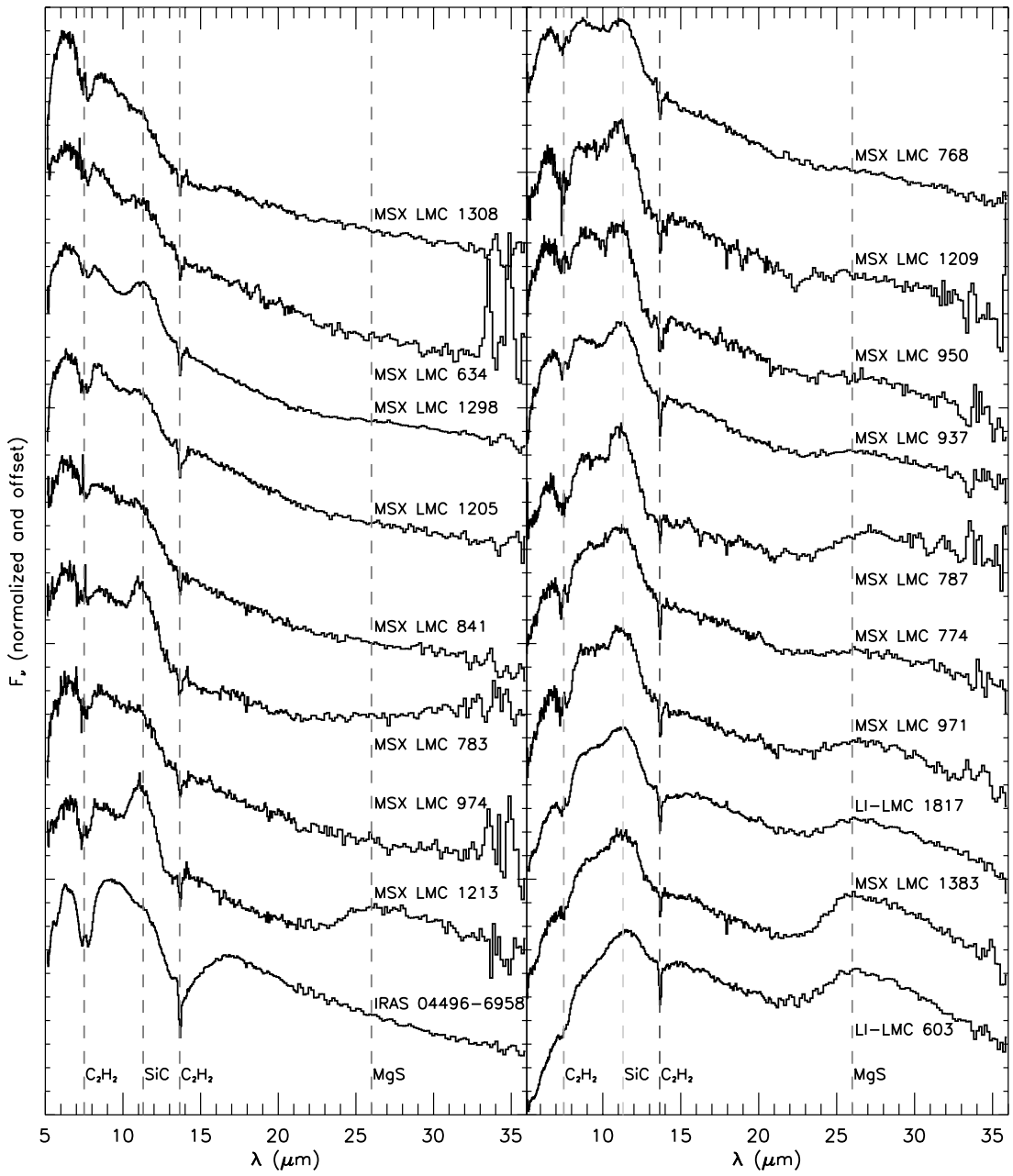

FIG. 1.—Our sample spectra of carbon-rich AGB stars observed in the LMC ranging from 5 to 36 μm. The spectra have been ordered by their [6.4] – [9.3] color from blue to red, normalized by the maximum value of their fitted blackbodies, and offset for clarity. The dashed lines indicate the positions of the C_2H_2 absorption features at 7.5 and 13.8 μm, the SiC emission features at 11.3 μm, and the MgS emission feature at ~26 μm.

11.3 μm generally attributed to SiC emission (Treffers & Cohen 1974). While the central wavelength of the SiC resonance as measured in the laboratory intrinsically lies at 11.3 μm (Gilra 1971), the central peak in astronomical data varies between 11.15 and 11.7 μm for Galactic sources. Speck et al. (2005) used grains of different sizes to interpret this shift: larger grains provide a cool absorbing component around 10.8 μm, while a warmer emitting component toward the red arises from smaller grains. Thus, different grain-size distributions will theoretically provide different contributions from emitting and absorbing components, causing the overall central wavelength of the SiC feature to shift.

2.2.4. MgS *Emission*

In slightly less than half of all the objects presented here, we observe a broad emission feature beginning blueward of 22 μm and extending beyond the IRS spectral range. This feature is commonly seen in carbon-rich AGB and post-AGB stars, as well as planetary nebulae, and consists of two subpeaks at 26 and 33 μm (Forrest et al. 1981), both of which are attributed to magnesium sulfide (MgS; Goebel & Moseley 1985). By calculating absorption cross sections for various grain shapes, Hony et al. (2002) modeled the MgS spectral feature of Galactic carbon stars and showed that the subpeaks are due to different distributions of grains shapes and that the peak wavelength of the feature shifts with temperature.

3. ANALYSIS

3.1. *Manchester Method*

Since the dominant component of the dust in these sources consists of featureless amorphous carbon (Martin & Rogers

TABLE 1
Observed LMC Targets

Adopted Name	R.A.(J2000.0)	Decl. (J2000.0)	2MASS[a]			*MSX* A[b]	AOR ID	Observation Date	Int. Time (s)	
			J	*H*	K_s				SL	LL
IRAS 04496−6958	04 49 18.50	−69 53 14.3	12.66	10.85	9.43	5.61	9069312	2004 Mar 1	112	240
LI-LMC 603	05 12 00.82	−70 32 24.0	18.04	16.77	14.52	5.51	6078464	2004 Mar 5	56	56
LI-LMC 1817	06 02 45.08	−67 22 43.0	18.43	16.23	13.53	6.08	6078208	2004 Apr 14	56	112
MSX LMC 1205	04 51 15.48	−68 41 40.3	14.97	12.84	11.09	7.11	11239168	2005 Mar 16	48	112
MSX LMC 1209	04 55 18.88	−68 46 30.7	16.64	14.94	12.74	7.03	11239168	2005 Mar 16	48	112
MSX LMC 1213	04 52 20.18	−68 43 30.1	17.98	14.85	12.44	7.08	11239168	2005 Mar 16	48	112
MSX LMC 1298	04 51 10.96	−69 20 14.7	15.50	13.05	11.12	5.92	11239168	2005 Mar 16	48	112
MSX LMC 1308	04 51 10.96	−69 20 14.7	14.23	12.32	10.82	5.90	11239168	2005 Mar 16	48	112
MSX LMC 1383	04 55 33.54	−69 24 59.3	18.11	15.85	13.08	5.90	11239424	2005 Mar 14	48	112
MSX LMC 634	05 26 35.70	−69 08 22.7	14.82	12.77	11.13	7.53	11238912	2005 Mar 16	48	112
MSX LMC 768	05 31 40.90	−69 39 19.8	15.83	13.20	11.06	5.99	11238912	2005 Mar 16	48	112
MSX LMC 774	05 26 23.10	−69 11 20.3	16.78	15.08	12.72	6.26	11238912	2005 Mar 16	48	112
MSX LMC 783	05 32 55.47	−69 20 26.6	15.85	13.65	11.73	7.00	11238912	2005 Mar 16	48	112
MSX LMC 787	05 34 56.21	−69 09 16.5	16.72	14.85	12.53	7.00	11238912	2005 Mar 16	48	112
MSX LMC 841	05 31 13.12	−66 09 41.2	15.78	13.40	11.55	7.07	11239680	2005 Mar 16	48	112
MSX LMC 937	05 40 36.06	−69 52 49.8	14.52	12.24	10.36	5.67	11239424	2005 Mar 14	48	112
MSX LMC 950	05 35 03.55	−69 52 45.5	14.78	12.47	10.65	6.75	11239424	2005 Mar 14	48	112
MSX LMC 971	05 39 51.85	−70 01 17.0	17.84	16.48	14.21	6.75	11239424	2005 Mar 14	48	112
MSX LMC 974	05 40 58.18	−69 53 12.7	14.45	12.54	10.98	7.12	11239424	2005 Mar 14	48	112

Note.—Observed LMC targets sorted alphabetically by the adopted name. Units of right ascension are hours, minutes, and seconds, and units of declination are degrees, arcminutes, and arcseconds, and are given in J2000.0. Photometry at *J*, *H*, and K_s is from 2MASS, and the A band (8.3 μm) is from the *MSX* survey. We also list the Astronomical Observation Request (AOR) ID, along with date of the observation and integration times for the short-low (SL) and long-low (LL) orders in terms of seconds.

[a] Skrutskie et al. (2006).

[b] Egan et al. (2001).

1987), it is useful to develop an observable quantity that represents the dust opacity. Previous analyses of carbon star data have utilized the "Manchester method" (Sloan et al. 2006) in order to define the amorphous carbon dust continuum amid the plentiful spectral emission and absorption features. This method defines four narrow bands centered at 6.4, 9.3, 16.5, and 21.5 μm that are used to determine a set of two color temperatures of [6.4] − [9.3] and [16.5] − [21.5]. These colors can then be used as proxies for the optical depth of the surrounding dust shell ($\tau \propto$ [6.4] − [9.3]) and for estimating the dust temperature, respectively.

A few complications arise when trying to perform this method on a sample of objects containing a wide range of dust temperatures. In particular, the Manchester 9.3 μm band fall directly within the 10 μm absorption feature, thus underestimating the dust continuum flux at this wavelength for stars with this feature (Fig. 2). However, this only affects a small number of the bluest objects providing a mean shift of 0.07 for the [6.4] − [9.3] color. Thus, we still rely on the [6.4] − [9.3] color to provide us with a qualitative analysis of the dust opacities. Furthermore, the 21.5 μm band, used to define the blackbody continuum, can acquire increased flux from the adjoining broad MgS feature for significant emission strengths, causing the continuum emission to be overestimated at these wavelengths. Prominent MgS emission can occur shortward of 20 μm for low dust temperatures (Hony et al. 2002).

In addition, the Manchester method adopts straight-line continuum fits in order to measure the strengths of the C_2H_2 absorption bands and the SiC emission feature. They defined wavelength segments of supposed continuum that flank the features of interest (see Sloan et al. 2006).

However, since the blue side of the continuum used for the SiC feature ranges from 9.5 to 10.1 μm, this method will tend to underestimate the underlying continuum and overestimate the flux in the SiC band (Fig. 2). Similarly, the varying strength of the C_2H_2 feature affects determination of the red side of the SiC feature.

In the most extreme cases, C_2H_2 absorption can reach as low as ~11 μm causing considerable suppression of the observed SiC emission. The same variation in broadness of the C_2H_2 bands also makes it difficult to set a consistent wavelength range at 7.5 and 14 μm that allows for proper isolation of the *P*-, *Q*-, and

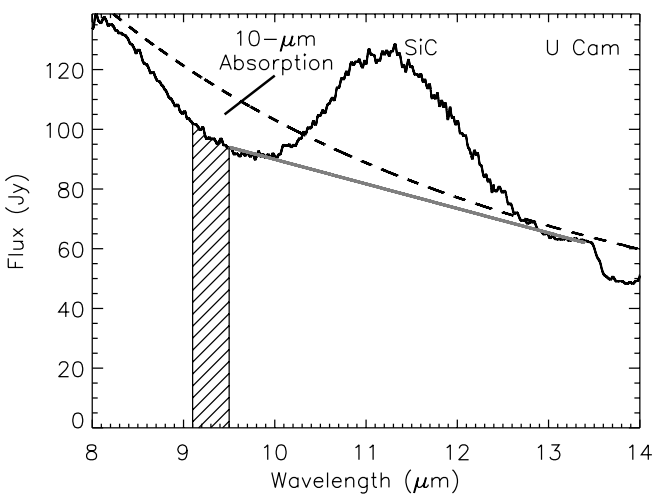

Fig. 2.—Spectra of U Cam showing the effect of the 10 μm absorption feature on the [9.3] Manchester band, represented as the cross-hatched vertical bar. The 10 μm band gives a flux value significantly below the probable continuum level, which is approximated by a modified blackbody. The resulting straight line continuum fit (*solid line*) differs significantly from the modified blackbody fit (*dashed line*) underneath the SiC emission. [*See the electronic edition of the Journal for a color version of this figure.*]

R-branches of C_2H_2. For this reason, previous studies only focused on the narrow Q-branch of the 13.7 μm feature and disregarded the flanking P- and R-branches. While this paper strives to improve on quantitative determinations of the various spectral features, we stress that our improvements described in the following section do not change the majority of the qualitative conclusions found by SZL using the Manchester method.

3.2. *Modified Blackbody Fits*

SZL employed the Manchester $[16.5]-[21.5]$ color to derive a blackbody color temperature and thereby extrapolate the continuum underneath the MgS feature. However, the aforementioned problems associated with this type of continuum estimation can lead to inaccurate determinations of dust properties such as the temperature, mass-loss rate, and total dust mass. We improve on this method by fitting a modified blackbody to each carbon star's spectrum. Expanding on the method described by Hony et al. (2002) we utilize a χ^2 fitting routine to find the best single-temperature modified blackbody to model the entire spectral continuum,

$$F(\lambda) = AB(\lambda, T)\lambda^{-p}, \quad (1)$$

where $F(\lambda)$ is the flux density of the continuum at some wavelength λ, $B(\lambda, T)$ is the Planck function with a temperature T, p is the dust emissivity index, and A is a scaling factor. We minimize the χ^2 values by varying the free parameters (T, p, and A) from equation (1) over selected continuum points. The p-parameter represents how efficiently the dust grains radiate at wavelengths larger than the grain size. To some extent, varying this parameter allows us to incorporate effects from optical depth and temperature gradients. Crystalline material has $p \sim 2$, amorphous material has an emissivity index between 1 and 2, and layered materials have $p \sim 1$. Temperature gradients within the dust shell lower the value of p by broadening the spectral energy distribution. Similarly, an optically thick dust shell further reduces the value of p.

For a source embedded in a circumstellar shell, one expects the continuum emission to follow the general form of

$$F_\nu(\lambda) = I_\nu(\lambda, T_\star)e^{-\tau_\nu} + B_\nu(\lambda, T_{\rm CS})(1 - e^{-\tau_\nu}), \quad (2)$$

where $I_\nu(\lambda, T_\star)$ is the stellar emission, d is the distance to the source, $B_\nu(\lambda, T_{\rm CS})$ is the blackbody emission of the circumstellar dust shell, τ_ν is the optical depth of the dust shell, and $T_\star$ and $T_{\rm CS}$ are the prevailing temperatures of the stellar photosphere and envelope, respectively. In cases where the optical depth is large at infrared wavelengths, the contribution from the stellar photosphere in equation (2) is negligible, and the modified blackbody fit (eq. [1]) gives an approximation for the average temperature of the dust shell. However, when the optical depth is small, the photospheric emission becomes important, and both $T_\star$ and $T_{\rm CS}$ contribute to the temperature in equation (1). For this case, the temperature T from the modified blackbody fit should be treated only as a fit parameter.

The blackbody continuum fits allow us to improve on straight-line continua by determining more precisely the wavelength range over which spectral features are present (Fig. 3).

In order to accommodate for the varying widths of the features, the continuum points were selected for each spectrum individually. We chose continuum points redward of the 7.5 μm C_2H_2 band between the 7.5 μm C_2H_2 band and SiC emission feature, and between the 14 μm C_2H_2 and MgS feature, taking care that none of the feature wings were included in the continuum selection. When fitting *ISO* spectra, the inclusion of wavelengths shortward of 5.2 μm that are unavailable in IRS spectra alters the best-fit temperature up to 10% and slightly shifts p toward negative values. In the majority of these cases, however, only minor differences arise in the temperature and p-value when considering the 2.3–5.2 μm region to constrain the continuum. Moreover, changes to the fitted continuum above and below the features of interest were imperceptible; therefore, we do not introduce a bias in the feature strengths of Galactic objects.

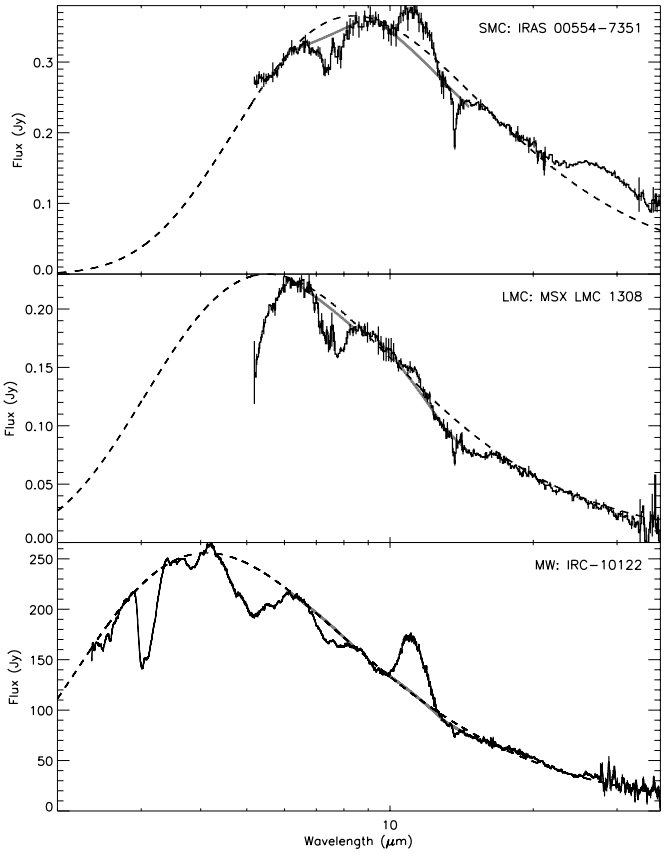

FIG. 3.—Example spectra with error bars of three sources, one from each environment—SMC, LMC, and the Milky Way from top to bottom. The dotted line indicates the χ^2 fits of the underlying carbon-rich dust continuum using a single-temperature modified blackbody. The straight line segments represent the estimated continuums using the method employed by SZL. We find the feature strengths by dividing the derived blackbody fits. [*See the electronic edition of the Journal for a color version of this figure.*]

In addition, we considered 2MASS J, H, and K_s points (Skrutskie et al. 2006) to constrain the shorter wavelengths of the blackbody points. However, due to the intrinsic variability of these objects, the 2MASS data points were only used to guide the slope of continuum fit rather than as rigid anchors. In addition, different dust temperatures dominate the emission between the near-IR 2MASS photometry and the mid-IR spectra, but we partially account for this effect with the inclusion of the dust emissivity index, p. Also, due to the relative distance and faintness of objects in the Magellanic Clouds as compared to objects in the Galaxy, spectral and photometric data for LMC and SMC objects contain larger uncertainties than Galactic objects. In the entire sample, 28 objects have a J-band magnitude greater than the 10 σ point-source detection limit of 15.8 mag, with 23 of these objects residing in the LMC. This number improves by half for the 10 σ H-band limit of 15.1 mag. Thus, using the 2MASS points as absolute constraints for the single-temperature blackbody fits was not recommended in every case.

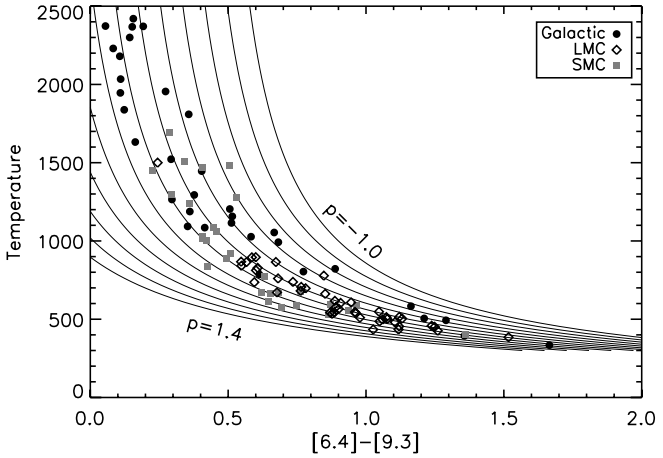

FIG. 4.—Contours of constant p-parameter values for modified blackbodies with temperatures ranging between 300 and 2500 K with $-1 \leq p \leq 1.4$ with a 0.2 increment. The symbols represent data from fitted blackbodies for the samples of Galactic, LMC, and SMC objects. Error bars for [6.4] − [9.3] are on the order of the symbol size. [*See the electronic edition of the Journal for a color version of this figure.*]

Figure 4 shows the result of equation (1) for modified blackbodies ranging from temperatures of 300–2500 K and p-values of −1.0 to 1.4. Continuous lines show how the temperature changes for varying [6.4] − [9.3] with constant p-values. We overplot the derived p- and T-values against the measured [6.4] − [9.3] values for the SMC, LMC, and Galactic samples. The mean p-values for the entire sample is 0.13 ± 0.26, and for the individual samples are 0.27 ± 0.2 (SMC), 0.18 ± 0.22 (LMC), and -0.05 ± 0.25 (Galactic). The variation in average values between the three environments may indicate a metallicity effect; however, since the p-parameter represents the optical properties of the grain which evolve over the lifetime of these objects, this may reflect the biases of each sample. For instance, the objects within the Milky Way contain the widest range of colors with the majority residing toward the blue, while the SMC sample contains the smallest color range and consists of much redder objects.

Due to the poor quality of some spectra, mispointings, and/or background contamination, we were unable to obtain blackbody fits for a total 11 objects from the various samples: *MSX* LMC 782 from our sample; NGC 1978 MIR1 and NGC 1978 IR4 (Zijlstra et al. 2006); NGC 419 LE 18, NGC 419 LE 27, NGC 419 LE 35, and ISO 00549 (Lagadec et al. 2007); and IRAS 18430−0237, S Lyr, SS73 38, and SZ Sgr (Sloan et al. 2003).

Table 2 lists the feature strengths determined using our modified blackbody fits. We measure equivalent widths of the 7.3 μm band, the 13.7 μm C_2H_2 Q-branch, and the P- and R-branches at 14 μm. Strengths of the dust emission features were determined by taking the ratio of the integrated flux to the integrated continuum. The central wavelength for the SiC feature was also found. We do not include features where low signal-to-noise ratios cause uncertainties comparable to the strength.

3.3. *Mass-Loss Rates*

Based on dust radiative transfer models, Groenewegen et al. (2007) determined dust and gas mass-loss rates for 60 carbon stars in the Magellanic Clouds, while Le Bertre (1997) modeled the circumstellar dust shells of 23 Galactic carbon stars. These works derived $\dot{M}_{\rm dust}$ directly from the infrared SEDs and NIR photometry. Gas mass-loss rates were subsequently derived by scaling by an assumed dust-to-gas ratio (ψ) based on the metallicity. Even though this is a common assumption when deriving $\dot{M}_{\rm gas}$, there are no studies that conclusively show that the total mass-loss rate explicitly depends on metallicity (Zijlstra et al. 1996). The dust-to-gas ratio has been shown to depend approximately linearly on initial metallicity, while mass-loss rate shows only a weak dependence (van Loon 2000). However, in order to proceed with our analysis of the dependencies of dust and molecular abundances with pressures and densities, we must make some assumption about the gas mass-loss rates.

When available, we use mass-loss rates published by Groenewegen et al. (2007) or Le Bertre (1997). In their derivation of $\dot{M}_{\rm gas}$, Groenewegen et al. (2007) used the same dust-to-gas ratio of $\psi = 0.005$ for all objects within the LMC and SMC. Instead, we have adopted $\psi = 0.002$ for SMC objects, corresponding to a metallicity of $Z = \frac{1}{5}\ Z_\odot$. This assumes that ψ scales with metallicity and $\psi_{\rm MW} = 0.01$.

For the objects within Magellanic Clouds, Groenewegen et al. (2007) show a correlation between $\dot{M}_{\rm dust}$ and the [6.4] − [9.3] color (Fig. 6*a*). The gas mass-loss rate for the LMC objects can then be derived by (van Loon 2007)

$$\log\left[\dot{M}_{\rm gas,\,LMC}\left(M_\odot\ {\rm yr}^{-1}\right)\right] = 2.55([6.4]-[9.3])^{0.5} - 7.6. \quad (3)$$

For the SMC sample, we modify equation (3) using a value of $\psi_{\rm SMC} = 0.002$,

$$\log\left[\dot{M}_{\rm gas,\,SMC}\left(M_\odot\ {\rm yr}^{-1}\right)\right] = 2.55([6.4]-[9.3])^{0.5} - 7.2. \quad (4)$$

Since these relations were derived only for objects in the range $0.2 \leq [6.4]-[9.3] \leq 1.5$, the mass-loss rates of objects with $[6.4]-[9.3] < 0.2$ are not well constrained, affecting 11 Galactic objects. Instead, we determined gas mass-loss for all Galactic objects using the relation from Le Bertre (1997)

$$\log\left[\dot{M}_{\rm gas,\,MW}\left(M_\odot\ {\rm yr}^{-1}\right)\right] = -6.0/(J-K-0.2) - 4.0, \quad (5)$$

assuming a dust-to-gas ratio of 0.01. We find a linear correlation between the $J-K$ and [6.4] − [9.3] colors for Galactic objects (Fig. 5). Therefore, we can overplot the trend from Le Bertre (1997) in terms of the [6.4] − [9.3] color. Figure 6 (*top*) shows that the dust mass-loss rates of the Galactic objects derived from 2MASS $J-K$ indeed overlap with those derived from the [6.4] − [9.3] color. Once we apply metallicity corrections for determining the gas mass-loss rates, objects in the separate samples no longer fall along a single trend (Fig. 6*b*). Table 3 lists the dust and gas mass-loss rates for each object.

4. RESULTS

4.1. *Acetylene Molecular Absorption*

4.1.1. *P- and R-Branches*

We plot the equivalent widths of the C_2H_2 bands at 7.5 and 14 μm as a function of the [6.4] − [9.3] color and $\dot{M}_{\rm gas}$ for the Galactic, LMC, and SMC samples in Figure 7. By plotting against the [6.4] − [9.3] color, we are comparing sources with the same optical depth. Assuming a constant expansion velocity independent of metallicity, the [6.4] − [9.3] color also directly correlates with the dust mass-loss rate assuming (Groenewegen et al. 2007). Matsuura et al. (2002) show that increasing the contribution from dust emission can affect the molecular band strength by filling in the C_2H_2 absorption and decreasing the equivalent width. Matsuura et al. (2005) and van Loon et al. (2006) show evidence of this "dust dilution" for C_2H_2 bands occurring at 3.1 and 3.8 μm in the Magellanic Clouds.

TABLE 2

SPECTROSCOPIC RESULTS

Name	[6.4] − [9.3] (mag)	EW(7.5) (μm)	EW(14) (μm)	EW(13.7) (μm)	L/C (SiC)	λ_{SiC} (μm)	L/C (MgS)
Our Sample							
IRAS 04496−6958	0.85 ± 0.00	0.337 ± 0.002	0.971 ± 0.007	0.112 ± 0.006	...	...	...
LI-LMC 603	1.52 ± 0.01	0.092 ± 0.002	0.152 ± 0.004	0.043 ± 0.002	0.042 ± 0.001	11.18 ± 0.05	0.426 ± 0.002
LI-LMC 1817	1.24 ± 0.01	0.179 ± 0.003	0.392 ± 0.004	0.054 ± 0.002	0.050 ± 0.001	11.11 ± 0.03	0.352 ± 0.002
MSX LMC 1205	0.67 ± 0.01	0.123 ± 0.002	0.103 ± 0.008	0.066 ± 0.005	0.045 ± 0.002	11.19 ± 0.07	...
MSX LMC 1209	0.87 ± 0.01	0.259 ± 0.006	0.232 ± 0.011	0.074 ± 0.007	0.124 ± 0.004	11.12 ± 0.04	...
MSX LMC 1213	0.77 ± 0.01	0.127 ± 0.003	0.114 ± 0.015	0.043 ± 0.013	0.159 ± 0.003	11.09 ± 0.03	0.481 ± 0.011
MSX LMC 1298	0.61 ± 0.01	0.066 ± 0.002	...	0.050 ± 0.003	0.106 ± 0.001	11.39 ± 0.02	0.083 ± 0.003
MSX LMC 1308	0.57 ± 0.01	0.181 ± 0.006	0.609 ± 0.013	0.041 ± 0.008	0.037 ± 0.007	10.07 ± 0.41	...
MSX LMC 1383	1.26 ± 0.01	0.176 ± 0.004	0.262 ± 0.007	0.026 ± 0.004	0.052 ± 0.002	11.21 ± 0.07	0.633 ± 0.005
MSX LMC 634	0.60 ± 0.01	0.078 ± 0.004	0.118 ± 0.012	0.055 ± 0.007	0.044 ± 0.003	11.34 ± 0.08	...
MSX LMC 768	0.85 ± 0.01	0.122 ± 0.002	0.191 ± 0.005	0.042 ± 0.003	0.085 ± 0.002	11.27 ± 0.03	0.072 ± 0.005
MSX LMC 774	1.08 ± 0.01	0.226 ± 0.004	0.273 ± 0.005	0.056 ± 0.003	0.075 ± 0.002	11.11 ± 0.06	0.349 ± 0.006
MSX LMC 783	0.68 ± 0.01	0.114 ± 0.003	0.271 ± 0.010	0.048 ± 0.008	0.128 ± 0.003	11.13 ± 0.04	...
MSX LMC 787	0.96 ± 0.01	0.195 ± 0.004	0.327 ± 0.011	0.023 ± 0.006	0.110 ± 0.003	11.10 ± 0.04	0.645 ± 0.096
MSX LMC 841	0.68 ± 0.01	0.141 ± 0.004	0.094 ± 0.008	0.047 ± 0.006	0.081 ± 0.003	11.06 ± 0.06	...
MSX LMC 937	0.91 ± 0.01	0.130 ± 0.002	0.109 ± 0.005	0.058 ± 0.003	0.101 ± 0.002	11.23 ± 0.03	0.278 ± 0.004
MSX LMC 950	0.88 ± 0.01	0.147 ± 0.004	0.361 ± 0.009	0.075 ± 0.006	0.112 ± 0.004	11.10 ± 0.05	0.287 ± 0.017
MSX LMC 971	1.12 ± 0.01	0.166 ± 0.005	0.433 ± 0.007	0.040 ± 0.005	0.069 ± 0.002	11.19 ± 0.04	0.422 ± 0.006
MSX LMC 974	0.74 ± 0.01	0.055 ± 0.005	0.223 ± 0.009	0.063 ± 0.006	0.049 ± 0.003	11.01 ± 0.08	...
Zijlstra et al. (2006) Sample							
GRRV 38	0.24 ± 0.03	0.384 ± 0.017	0.237 ± 0.032	0.135 ± 0.023	0.173 ± 0.016	11.17 ± 0.08	...
IRAS 04557−6753	1.07 ± 0.01	0.218 ± 0.006	0.195 ± 0.007	0.060 ± 0.003	0.091 ± 0.004	11.21 ± 0.07	0.461 ± 0.004
IRAS 05009−6616	0.90 ± 0.00	0.084 ± 0.002	0.111 ± 0.004	0.051 ± 0.002	0.122 ± 0.001	11.21 ± 0.02	0.267 ± 0.003
IRAS 05112−6755	1.12 ± 0.01	0.180 ± 0.003	0.386 ± 0.004	0.058 ± 0.002	0.052 ± 0.001	11.08 ± 0.04	0.317 ± 0.002
IRAS 05113−6739	1.05 ± 0.02	0.187 ± 0.004	0.085 ± 0.007	0.044 ± 0.005	0.066 ± 0.002	11.23 ± 0.08	0.299 ± 0.004
IRAS 05132−6941	1.05 ± 0.01	0.154 ± 0.004	0.219 ± 0.010	0.062 ± 0.007	0.094 ± 0.006	11.24 ± 0.08	0.138 ± 0.006
IRAS 05190−6748	1.25 ± 0.01	0.172 ± 0.003	0.251 ± 0.006	0.063 ± 0.004	0.044 ± 0.005	11.15 ± 0.20	0.418 ± 0.001
IRAS 05278−6942	1.11 ± 0.01	0.135 ± 0.004	0.295 ± 0.009	0.074 ± 0.007	0.067 ± 0.005	11.02 ± 0.12	0.502 ± 0.002
IRAS 05295−7121	0.95 ± 0.01	0.108 ± 0.004	0.139 ± 0.007	0.063 ± 0.004	0.066 ± 0.003	11.20 ± 0.07	0.169 ± 0.003
IRAS 05360−6648	1.06 ± 0.01	0.157 ± 0.004	0.279 ± 0.007	0.042 ± 0.004	0.125 ± 0.003	11.07 ± 0.04	0.691 ± 0.005
MSX LMC 219	1.13 ± 0.01	0.256 ± 0.003	0.541 ± 0.006	0.048 ± 0.004	0.048 ± 0.002	11.18 ± 0.05	0.384 ± 0.004
MSX LMC 341	0.96 ± 0.01	0.142 ± 0.006	0.166 ± 0.007	0.050 ± 0.003	0.124 ± 0.002	11.01 ± 0.03	0.672 ± 0.008
MSX LMC 349	0.98 ± 0.01	0.113 ± 0.003	0.322 ± 0.007	0.045 ± 0.003	0.122 ± 0.003	11.04 ± 0.04	0.740 ± 0.008
MSX LMC 441	1.12 ± 0.01	0.195 ± 0.005	0.407 ± 0.007	0.046 ± 0.004	0.082 ± 0.002	11.07 ± 0.03	0.647 ± 0.004
MSX LMC 443	0.89 ± 0.01	0.261 ± 0.004	0.364 ± 0.009	0.037 ± 0.006	0.119 ± 0.003	11.11 ± 0.03	0.534 ± 0.004
MSX LMC 494	0.55 ± 0.01	0.186 ± 0.003	0.065 ± 0.004	0.036 ± 0.003	0.095 ± 0.002	11.23 ± 0.03	...
MSX LMC 601	0.89 ± 0.01	0.035 ± 0.003	0.109 ± 0.005	0.055 ± 0.003	0.043 ± 0.003	11.11 ± 0.11	...
MSX LMC 679	0.89 ± 0.01	0.161 ± 0.003	0.267 ± 0.008	0.035 ± 0.005	0.131 ± 0.005	11.07 ± 0.07	0.534 ± 0.003
MSX LMC 743	1.03 ± 0.01	0.279 ± 0.004	0.425 ± 0.007	0.028 ± 0.004	0.107 ± 0.003	11.11 ± 0.04	0.701 ± 0.003
MSX LMC 749	0.60 ± 0.01	0.146 ± 0.003	0.320 ± 0.008	0.067 ± 0.005	0.063 ± 0.006	11.02 ± 0.15	...
MSX LMC 754	0.60 ± 0.02	0.122 ± 0.004	0.554 ± 0.012	0.013 ± 0.008	0.132 ± 0.004	11.10 ± 0.04	...
MSX LMC 967	0.59 ± 0.01	0.055 ± 0.004	0.168 ± 0.012	0.062 ± 0.011	0.065 ± 0.006	11.23 ± 0.21	...
NGC 1978 IR1	0.55 ± 0.01	0.122 ± 0.002	0.383 ± 0.007	0.057 ± 0.003	0.088 ± 0.002	11.08 ± 0.05	...
TRM 72	0.78 ± 0.01	0.051 ± 0.004	0.121 ± 0.007	0.069 ± 0.004	0.064 ± 0.002	11.18 ± 0.05	...
TRM 88	0.76 ± 0.02	0.121 ± 0.006	0.178 ± 0.006	0.055 ± 0.003	0.058 ± 0.007	10.97 ± 0.13	...
Sloan et al. (2006) Sample							
MSX SMC 033	0.51 ± 0.01	0.052 ± 0.002	0.081 ± 0.006	0.050 ± 0.003	0.059 ± 0.002	10.96 ± 0.06	...
MSX SMC 036	0.76 ± 0.01	0.299 ± 0.005	0.401 ± 0.008	0.054 ± 0.005	0.042 ± 0.002	11.06 ± 0.04	...
MSX SMC 044	0.53 ± 0.01	0.041 ± 0.003	...	0.066 ± 0.008	0.079 ± 0.003	10.98 ± 0.07	...
MSX SMC 054	0.75 ± 0.01	0.236 ± 0.002	0.209 ± 0.006	0.057 ± 0.004	0.139 ± 0.001	11.19 ± 0.01	0.177 ± 0.020
MSX SMC 060	0.96 ± 0.00	0.215 ± 0.003	...	0.037 ± 0.003	0.030 ± 0.002	11.27 ± 0.08	0.228 ± 0.027
MSX SMC 062	0.65 ± 0.02	0.129 ± 0.006	0.055 ± 0.012	0.053 ± 0.007	0.055 ± 0.003	11.13 ± 0.09	...
MSX SMC 066	0.43 ± 0.01	0.091 ± 0.002	0.464 ± 0.012	0.040 ± 0.004	0.025 ± 0.002	11.24 ± 0.04	...
MSX SMC 091	0.65 ± 0.02	0.358 ± 0.010	0.329 ± 0.022	0.059 ± 0.017	0.121 ± 0.007	11.23 ± 0.07	...
MSX SMC 093	0.46 ± 0.01	0.241 ± 0.004	1.077 ± 0.014	0.027 ± 0.008	0.016 ± 0.003	10.81 ± 0.11	...
MSX SMC 105	0.87 ± 0.01	0.297 ± 0.004	0.085 ± 0.006	0.029 ± 0.004	0.120 ± 0.003	11.12 ± 0.04	0.487 ± 0.014
MSX SMC 142	0.29 ± 0.03	0.165 ± 0.007	...	0.090 ± 0.030	0.131 ± 0.016	11.56 ± 0.28	...
MSX SMC 159	0.87 ± 0.01	0.204 ± 0.002	0.285 ± 0.005	0.047 ± 0.004	0.124 ± 0.001	11.04 ± 0.02	0.417 ± 0.010
MSX SMC 162	0.50 ± 0.01	0.091 ± 0.004	0.393 ± 0.016	0.006 ± 0.011	0.078 ± 0.004	11.09 ± 0.10	...

TABLE 2—*Continued*

Name	[6.4] − [9.3] (mag)	EW(7.5) (μm)	EW(14) (μm)	EW(13.7) (μm)	L/C (SiC)	λ_{SiC} (μm)	L/C (MgS)
Sloan et al. (2006) Sample							
MSX SMC 163	0.68 ± 0.01	0.171 ± 0.003	0.276 ± 0.006	0.054 ± 0.003	0.119 ± 0.002	11.15 ± 0.02	0.236 ± 0.008
MSX SMC 198	0.62 ± 0.01	0.141 ± 0.003	0.009 ± 0.011	0.073 ± 0.005	0.055 ± 0.002	11.10 ± 0.05	...
MSX SMC 200	0.42 ± 0.01	0.007 ± 0.003	0.095 ± 0.007	0.069 ± 0.005	...	...	...
MSX SMC 202	0.45 ± 0.02	0.158 ± 0.006	0.078 ± 0.019	0.002 ± 0.017	0.037 ± 0.007	10.65 ± 0.23	...
MSX SMC 209	0.70 ± 0.01	0.198 ± 0.002	0.350 ± 0.007	0.047 ± 0.003	...	...	...
MSX SMC 232	0.63 ± 0.01	0.100 ± 0.002	0.270 ± 0.009	0.061 ± 0.004	0.009 ± 0.002	10.92 ± 0.15	...
Lagadec et al. (2007) Sample							
GM780	0.41 ± 0.01	0.340 ± 0.010	0.164 ± 0.024	0.035 ± 0.016	0.246 ± 0.007	11.07 ± 0.05	...
IRAS 00554−7351	0.94 ± 0.01	0.145 ± 0.005	0.186 ± 0.009	0.078 ± 0.007	0.085 ± 0.005	11.27 ± 0.09	0.291 ± 0.004
ISO 00548	0.41 ± 0.01	0.060 ± 0.003	0.023 ± 0.008	0.064 ± 0.005	0.086 ± 0.002	11.30 ± 0.03	...
ISO 00573	0.30 ± 0.01	0.167 ± 0.006	0.197 ± 0.013	0.078 ± 0.008	0.007 ± 0.007	11.72 ± 0.56	...
ISO 01019	0.41 ± 0.02	0.137 ± 0.004	0.001 ± 0.012	0.039 ± 0.009	0.056 ± 0.005	11.25 ± 0.10	...
LEGC 105	0.36 ± 0.02	0.094 ± 0.002	0.198 ± 0.010	0.054 ± 0.005	0.044 ± 0.003	11.09 ± 0.07	...
NGC 419 IR1	0.49 ± 0.01	0.152 ± 0.002	0.766 ± 0.008	0.041 ± 0.004	...	...	...
NGC 419 LE 16	0.34 ± 0.02	0.090 ± 0.004	0.185 ± 0.016	0.066 ± 0.012	0.071 ± 0.004	11.23 ± 0.06	...
NGC 419 MIR1	1.36 ± 0.01	0.278 ± 0.005	0.500 ± 0.007	0.048 ± 0.004	0.023 ± 0.003	11.40 ± 0.13	0.409 ± 0.003
RAW 960	0.23 ± 0.01	0.226 ± 0.004	0.141 ± 0.026	0.064 ± 0.009	0.063 ± 0.005	11.17 ± 0.09	...
Sloan et al. (2003) Sample							
AFGL 2392	0.58 ± 0.00	0.081 ± 0.001	0.028 ± 0.002	0.022 ± 0.001	0.312 ± 0.000	11.19 ± 0.00	0.336 ± 0.002
AFGL 3099	1.21 ± 0.00	0.063 ± 0.001	0.008 ± 0.001	0.067 ± 0.001	0.130 ± 0.000	11.43 ± 0.00	0.427 ± 0.001
AFGL 341	1.67 ± 0.01	0.080 ± 0.001	0.042 ± 0.001	0.050 ± 0.001	0.032 ± 0.000	12.12 ± 0.01	0.318 ± 0.001
AFGL 940	0.77 ± 0.00	0.040 ± 0.001	0.010 ± 0.003	0.041 ± 0.002	0.176 ± 0.001	11.27 ± 0.01	0.311 ± 0.002
C 2178	0.42 ± 0.00	0.155 ± 0.001	0.158 ± 0.004	0.041 ± 0.002	0.200 ± 0.001	11.23 ± 0.01	...
C 2429	0.19 ± 0.00	0.166 ± 0.001	...	0.032 ± 0.002	0.614 ± 0.001	11.36 ± 0.00	...
Case 181	0.61 ± 0.00	0.047 ± 0.001	0.081 ± 0.001	0.052 ± 0.001	0.199 ± 0.000	11.25 ± 0.00	0.186 ± 0.000
DO 16793	1.29 ± 0.00	0.043 ± 0.000	0.252 ± 0.001	0.048 ± 0.001	0.078 ± 0.000	11.30 ± 0.01	0.454 ± 0.000
DO 40123	0.29 ± 0.00	0.311 ± 0.001	0.101 ± 0.002	0.057 ± 0.001	0.275 ± 0.000	11.08 ± 0.00	...
HV Cas	0.35 ± 0.00	0.146 ± 0.000	0.004 ± 0.002	0.043 ± 0.001	0.216 ± 0.000	11.34 ± 0.00	...
IRAS 21489+5301	1.36 ± 0.01	0.102 ± 0.001	0.072 ± 0.002	0.044 ± 0.002	0.018 ± 0.001	12.09 ± 0.02	0.347 ± 0.001
IRC+00365	0.67 ± 0.00	0.077 ± 0.000	...	0.032 ± 0.001	0.178 ± 0.000	11.32 ± 0.00	0.206 ± 0.000
IRC+20326	0.89 ± 0.00	0.009 ± 0.001	0.030 ± 0.001	0.003 ± 0.000	0.078 ± 0.000	11.44 ± 0.01	0.354 ± 0.000
IRC+40540	1.16 ± 0.00	0.064 ± 0.000	0.001 ± 0.000	0.036 ± 0.000	0.148 ± 0.000	11.33 ± 0.00	0.310 ± 0.000
IRC+50096	0.68 ± 0.00	0.111 ± 0.001	0.246 ± 0.001	0.031 ± 0.001	0.257 ± 0.000	11.13 ± 0.00	0.144 ± 0.000
IRC−10095	0.16 ± 0.00	0.292 ± 0.001	...	0.013 ± 0.002	0.140 ± 0.001	11.35 ± 0.01	...
IRC−10122	0.38 ± 0.00	0.093 ± 0.000	0.140 ± 0.003	0.031 ± 0.001	0.243 ± 0.000	11.15 ± 0.00	...
RU Vir	0.51 ± 0.00	0.076 ± 0.001	0.085 ± 0.001	0.011 ± 0.001	0.320 ± 0.000	11.08 ± 0.00	...
RY Dra	0.11 ± 0.00	0.115 ± 0.000	...	0.081 ± 0.001	0.099 ± 0.000	11.61 ± 0.00	...
R For	0.36 ± 0.00	0.142 ± 0.001	0.073 ± 0.002	0.023 ± 0.001	0.264 ± 0.000	11.13 ± 0.00	...
R Scl	0.27 ± 0.00	0.390 ± 0.001	0.712 ± 0.003	0.077 ± 0.001	0.154 ± 0.001	11.09 ± 0.00	...
SS Vir	0.36 ± 0.00	0.420 ± 0.000	0.274 ± 0.009	0.058 ± 0.004	0.317 ± 0.001	11.17 ± 0.00	...
S Cep	0.30 ± 0.00	0.160 ± 0.000	...	0.045 ± 0.001	0.253 ± 0.001	11.15 ± 0.01	...
S Sct	0.14 ± 0.00	0.293 ± 0.001	0.022 ± 0.002	0.098 ± 0.002	0.160 ± 0.000	11.15 ± 0.01	...
TU Tau	0.08 ± 0.00	...	...	0.128 ± 0.007	0.270 ± 0.001	11.44 ± 0.01	...
T Dra	0.51 ± 0.00	0.162 ± 0.001	0.137 ± 0.003	0.026 ± 0.001	0.344 ± 0.000	11.07 ± 0.00	0.149 ± 0.002
U Cam	0.11 ± 0.00	0.065 ± 0.000	0.095 ± 0.002	0.075 ± 0.001	0.279 ± 0.000	11.34 ± 0.00	...
V460 Cyg	0.16 ± 0.00	0.125 ± 0.000	0.067 ± 0.004	0.077 ± 0.003	0.049 ± 0.001	11.56 ± 0.02	...
VX And	0.12 ± 0.00	0.214 ± 0.000	0.260 ± 0.004	0.101 ± 0.002	0.115 ± 0.000	11.39 ± 0.00	...
V Aql	0.11 ± 0.00	0.146 ± 0.001	0.156 ± 0.002	0.097 ± 0.001	0.098 ± 0.000	11.38 ± 0.00	...
V CrB	0.40 ± 0.00	0.166 ± 0.001	0.180 ± 0.003	0.053 ± 0.001	0.387 ± 0.000	11.12 ± 0.00	0.140 ± 0.005
V Cyg	0.52 ± 0.00	0.196 ± 0.000	0.351 ± 0.003	0.036 ± 0.001	0.309 ± 0.000	11.01 ± 0.00	0.060 ± 0.001
W Ori	0.06 ± 0.00	0.058 ± 0.000	0.006 ± 0.001	0.082 ± 0.001	0.144 ± 0.000	11.47 ± 0.00	...
Y CVn	0.15 ± 0.00	0.179 ± 0.001	0.029 ± 0.002	0.067 ± 0.002	0.068 ± 0.000	11.50 ± 0.01	...

NOTES.—For all objects in each sample, we show the [6.4] − [9.3] color, as well as strengths of the molecular and dust features. The molecular features are measured in terms of equivalent widths (EW) in microns, while the dust emission bands show a line-to-continuum ratio (L/C). We also give the central wavelength of the SiC feature (λ_{SiC}).

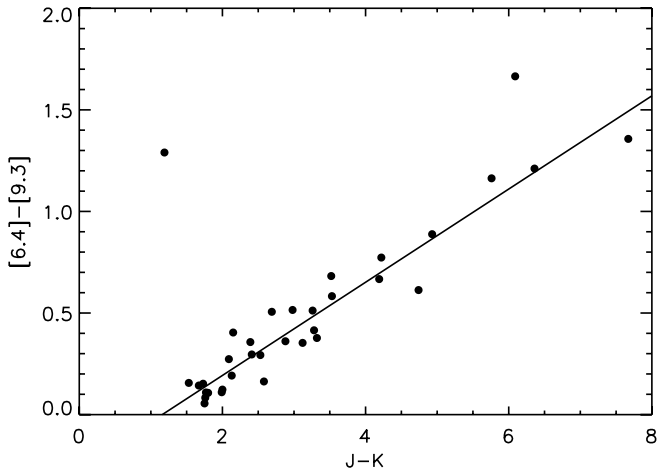

FIG. 5.—Correlation between 2MASS $J - K$ and [6.4] – [9.3] colors for Galactic objects. We have overplotted the best-fit linear relation. [*See the electronic edition of the Journal for a color version of this figure.*]

Analyzing the Galactic sample, we find that the 7.5 μm band shows a behavior similar to the 3.8 μm C_2H_2 bands from Matsuura et al. (2005). Figures 7*a* and 7*b* show an initial increase in equivalent width with optical depth and mass-loss rate, indicating a rise in level populations from increasing pressure and density. Circumstellar emission subsequently fills in the absorption band at $\dot{M}_{\rm gas} \sim 10^{-6.5}$, causing a decline in the equivalent width. The 7.5 μm absorption feature reflects this trend better than the 14 μm band, since the SiC emission feature tends to overlap the 14 μm *P*-branch.

The *P*- and *R*-branch acetylene bands also show a dependence on metallicity. For a given [6.4] – [9.3] color, objects from the SMC sample show slightly larger equivalent widths than those from the LMC. This is even more pronounced when compared to Galactic sources at 7.5 and 14 μm, albeit with considerable scatter (Figs. 7*a* and 7*c*). However, plotted against gas mass-loss rate, those objects from the LMC and SMC occupy the same space (Figs. 7*b* and 7*d*). Our assumptions when deriving gas mass-loss rates effectively discard the metallicity dependence between the LMC and SMC objects found by Lagadec et al. (2007) when using different and equally valid assumptions. Thus, we must be aware that the assumptions we make affect qualitative results when dealing with the gas mass-loss rates. However, the LMC and SMC objects show significantly higher equivalent widths than their Galactic counterparts with the same $\dot{M}_{\rm gas}$ as found by SZL. These works suggest that efficient dredge-ups for low-metallicity C stars help to increase the C/O ratio and, therefore, the C_2H_2 equivalent width for these bands. In addition, for a given $\dot{M}_{\rm gas}$, objects in the Magellanic Clouds will contain less dust than Galactic objects, causing effects from dust dilution to be less pronounced for the SMC and LMC samples.

4.1.2. 13.7 μm *Q-Branch*

Figure 8 shows the equivalent width of the *Q*-branch band at 13.7 μm as a function of the [6.4] – [9.3] color and $\dot{M}_{\rm gas}$. For Galactic objects, we observe a trend of the 13.7 μm *Q*-branch equivalent width with mass-loss rate. The equivalent width initially decreases until [6.4] – [9.3] = 0.5 and $\dot{M}_{\rm gas} = 10^{-6}\,M_\odot\ {\rm yr}^{-1}$ then very slightly increases. Van Loon et al. (2006) observe similar trends in absorption bands at 3.1, 3.57, 3.7, and 3.8 μm and explain them as being due to a competition between the effect of dust dilution and the effect of higher densities from an increasing mass-loss rate. The initial decline toward red colors in the Galactic sample suggests that circumstellar dust emission fills in the absorption feature. As gas mass-loss rate and pressure increase, densities become sufficiently high to overcome effects from the veiling at around $10^{-6}\ M_\odot\ {\rm yr}^{-1}$ and effectively increase the 13.7 μm equivalent width. This would suggest that the 13.7 μm C_2H_2 band has a stronger dependence on the gas density than the dust column density at higher $\dot{M}_{\rm gas}$.

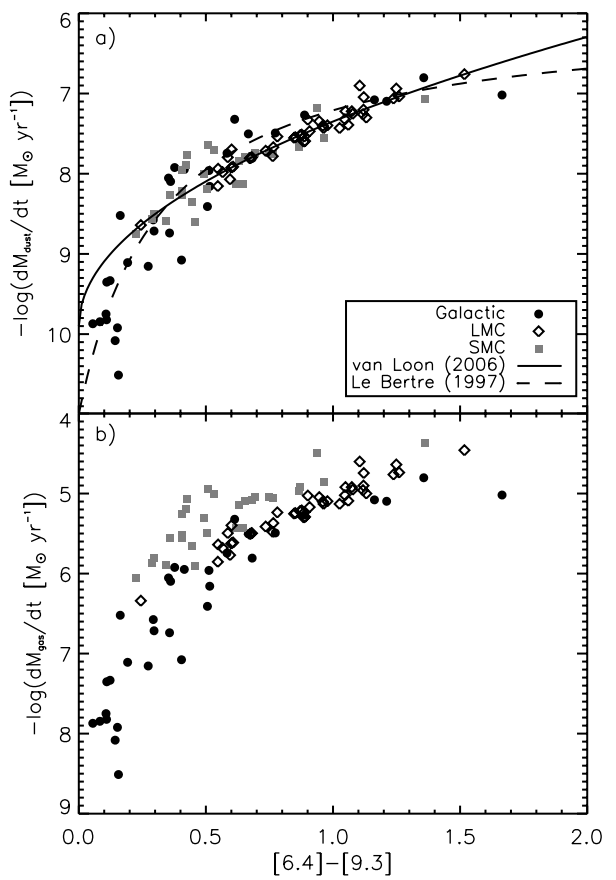

FIG. 6.—Plots of the mass-loss rates derived from eq. (3)–(5) with respect to the [6.4] – [9.3] color. The top panel shows that $\dot{M}_{\rm dust}$ derived for the objects in the Milky Way from $J - K$ (Le Bertre 1997) correlates with those approximated from the [6.4] – [9.3] color (van Loon 2007). Due to difference in assumed dust-to-gas ratios, each metallicity environment has a slightly different correlation between the gas mass-loss rate and the [6.4] – [9.3] color. [*See the electronic edition of the Journal for a color version of this figure.*]

We observe a similar trend of initially decreasing 13.7 μm equivalent width for SMC objects in Figure 8*a* at [6.4] – [9.3] < 0.5, which overlaps the Galactic trend. However, when plotted against $\dot{M}_{\rm gas}$, these particular objects no longer correspond to the observed Galactic trend, supporting the interpretation that dust dilution has a prominent influence on the 13.7 μm absorption at lower mass-loss rates. Such a trend is not observed for the LMC sample, since only one object (GRRV 38) has a value of [6.4] – [9.3] less than 0.5. At $\dot{M}_{\rm gas} \gtrsim 10^{-6}\,M_\odot\ {\rm yr}^{-1}$, however, the slightly increasing trend of the Galactic objects is generally matched by both the LMC and SMC objects. This further suggests that effects from increasing densities dominate over effects from dust dilution at higher gas mass-loss rates for this absorption band.

Figure 5 of Matsuura et al. (2006) show the same increase in the 13.7 μm equivalent width with [6.4] – [9.3] color and interpret this as evidence for a lack of dust dilution. However, except for one star, their entire sample consists of objects redder than [6.4] – [9.3] = 0.5 with $\dot{M}_{\rm gas} \gtrsim 10^{-5.5}\ M_\odot\ {\rm yr}^{-1}$; therefore, they were unable to observe the initial decrease in the equivalent width.

TABLE 3
MASS-LOSS RATES

Name	$\log \dot{M}_{\rm dust}$[a] ($M_\odot$ yr^{-1})	$\log \dot{M}_{\rm gas}$[b] ($M_\odot$ yr^{-1})	$\dot{M}_{\rm dust}$ Ref.	Type[c]	Type Ref.	Name	$\log \dot{M}_{\rm dust}$[a] ($M_\odot$ yr^{-1})	$\log \dot{M}_{\rm gas}$[b] ($M_\odot$ yr^{-1})	$\dot{M}_{\rm dust}$ Ref.	Type[c]	Type Ref.
Our Sample						Our Sample					
IRAS 04496−6958	−7.55	−5.25	1	...	...	MSX LMC 768	−7.55	−5.25	1	...	...
LI-LMC 603	−6.76	−4.46	1	...	...	MSX LMC 774	−7.25	−4.95	1	...	...
LI-LMC 1817	−7.06	−4.76	1	...	...	MSX LMC 783	−7.80	−5.50	1	...	...
MSX LMC 1205	−7.81	−5.51	1	...	...	MSX LMC 787	−7.40	−5.10	1	...	...
MSX LMC 1209	−7.52	−5.22	1	...	...	MSX LMC 841	−7.80	−5.50	1	...	...
MSX LMC 1213	−7.67	−5.37	1	...	...	MSX LMC 937	−7.47	−5.17	1	...	...
MSX LMC 1298	−7.91	−5.61	1	...	...	MSX LMC 950	−7.51	−5.21	1	...	...
MSX LMC 1308	−7.98	−5.68	1	...	...	MSX LMC 971	−7.20	−4.90	1	...	...
MSX LMC 1383	−7.04	−4.74	1	...	...	MSX LMC 974	−7.71	−5.41	1	...	...
MSX LMC 634	−7.93	−5.62	1	...	...	...	...	...	...	...	...
Zijlstra et al. (2006) Sample						Zijlstra et al. (2006) Sample					
GRRV 38	−8.64	−6.34	1	R	2	MSX LMC 441	−7.26	−4.96	2	R	2
IRAS 04557−6753	−7.22	−4.92	2	N	2	MSX LMC 443	−7.60	−5.30	2	R	2
IRAS 05009−6616	−7.33	−5.03	2	N	2	MSX LMC 494	−8.15	−5.85	2	R	2
IRAS 05112−6755	−7.05	−4.74	2	N	2	MSX LMC 601	−7.59	−5.29	2	R	2
IRAS 05113−6739	−7.22	−4.92	2	N	2	MSX LMC 679	−7.54	−5.24	2	R	2
IRAS 05132−6941	−7.32	−5.02	2	R	2	MSX LMC 743	−7.43	−5.13	2	R	2
IRAS 05190−6748	−6.94	−4.64	2	N	2	MSX LMC 749	−7.70	−5.40	2	R	2
IRAS 05278−6942	−6.90	−4.60	2	R	2	MSX LMC 754	−8.07	−5.77	2	R	2
IRAS 05295−7121	−7.35	−5.05	2	N	2	MSX LMC 967	−7.80	−5.49	2	R	2
IRAS 05360−6648	−7.39	−5.09	2	N	2	NGC 1978 IR1	−7.94	−5.64	2	N	2
MSX LMC 219	−7.30	−5.00	2	R	2	TRM 72	−7.54	−5.24	2	N	2
MSX LMC 341	−7.43	−5.13	2	R	2	TRM 88	−7.78	−5.48	2	R	2
MSX LMC 349	−7.40	−5.10	2	R	2	...	...	...	...	...	...
Sloan et al. (2006) Sample						Sloan et al. (2006) Sample					
MSX SMC 033	−7.65	−4.95	2	R	2	MSX SMC 142	−8.57	−5.87	2	R	2
MSX SMC 036	−7.76	−5.06	2	N	2	MSX SMC 159	−7.62	−4.92	2	N	2
MSX SMC 044	−7.70	−5.00	2	R	2	MSX SMC 162	−8.19	−5.49	2	N	2
MSX SMC 054	−7.74	−5.05	2	...	...	MSX SMC 163	−7.78	−5.08	2	R	2
MSX SMC 060	−7.55	−4.85	2	N	2	MSX SMC 198	−8.12	−5.43	2	R	2
MSX SMC 062	−7.80	−5.10	2	R	2	MSX SMC 200	−7.89	−5.19	2	...	...
MSX SMC 066	−7.77	−5.07	2	N	2	MSX SMC 202	−8.36	−5.66	2	...	...
MSX SMC 091	−8.12	−5.43	2	...	...	MSX SMC 209	−7.74	−5.05	2	R	2
MSX SMC 093	−8.60	−5.90	2	...	...	MSX SMC 232	−7.84	−5.14	2	N	2
MSX SMC 105	−7.67	−4.97	2	R	2	...	...	...	...	...	...
Lagadec et al. (2007) Sample						Lagadec et al. (2007) Sample					
GM780	−8.22	−5.52	2	R	2	LEGC 105	−8.26	−5.56	2	R	2
IRAS 00554−7351	−7.19	−4.49	2	N	2	NGC 419 IR1	−8.00	−5.30	2	N	2
ISO 00548	−7.96	−5.26	2	R	2	NGC 419 LE 16	−8.59	−5.89	2	N	2
ISO 00573	−8.51	−5.81	2	R	2	NGC 419 MIR1	−7.07	−4.37	2	R	2
ISO 01019	−8.26	−5.56	2	R	2	RAW 960	−8.76	−6.06	2	R	2

TABLE 3—*Continued*

Name	$\log \dot{M}_{\rm dust}$[a] ($M_\odot$ yr^{-1})	$\log \dot{M}_{\rm gas}$[b] ($M_\odot$ yr^{-1})	$\dot{M}_{\rm dust}$ Ref.	Type[c]	Type Ref.	Name	$\log \dot{M}_{\rm dust}$[a] ($M_\odot$ yr^{-1})	$\log \dot{M}_{\rm gas}$[b] ($M_\odot$ yr^{-1})	$\dot{M}_{\rm dust}$ Ref.	Type[c]	Type Ref.
Sloan et al. (2003) Sample						Sloan et al. (2003) Sample					
AFGL 2392	−7.74	−5.74	3	M	5	RU Vir	−7.96	−5.96	4	M	7
AFGL 3099	−7.10	−5.10	3	M	6	RY Dra	−9.82	−7.82	4	S	7
AFGL 341	−7.02	−5.02	4	M	6	R For	−8.10	−6.10	3	M	7
AFGL 940	−7.49	−5.49	4	...	...	R Scl	−9.15	−7.15	3	S	7
C 2178	−7.95	−5.95	4	...	...	SS Vir	−8.74	−6.74	4	S	7
C 2429	−9.11	−7.11	4	I	7	S Cep	−8.71	−6.71	4	M	7
Case 181	−7.32	−5.32	4	I	6	S Sct	−10.08	−8.08	4	S	7
DO 16793	−12.06	−10.06	4	...	...	TU Tau	−9.85	−7.85	4	S	7
DO 40123	−8.58	−6.58	4	M	6	T Dra	−8.41	−6.41	4	M	7
HV Cas	−8.05	−6.05	4	M	5	U Cam	−9.75	−7.75	4	S	7
IRAS 21489+5301	−6.80	−4.80	4	...	...	V460 Cyg	−10.51	−8.51	4	S	7
IRC+00365	−7.50	−5.50	4	M	6	VX And	−9.33	−7.33	4	S	7
IRC+20326	−7.27	−5.27	4	...	...	V Aql	−9.35	−7.35	4	S	7
IRC+40540	−7.08	−5.08	4	M	7	V CrB	−9.08	−7.08	4	M	7
IRC+50096	−7.81	−5.81	4	M	7	V Cyg	−8.16	−6.16	4	M	7
IRC−10095	−8.52	−6.52	4	...	...	W Ori	−9.87	−7.87	4	S	7
IRC−10122	−7.92	−5.92	4	M	6	Y CVn	−9.92	−7.92	4	S	7

[a] Dust mass-loss rates are either results of dust radiative transfer models of a given source or taken from relations based off of these models.
[b] Gas mass-loss rates were derived using eqs. (3)–(5).
[c] Objects in the LMC and SMC exhibit Mira-like pulsations: R stands for regular pulsation, and N stands for nonregular pulsation. For Galactic objects, M stands for Mira, I stands for irregular, and S stands for semiregular.

REFERENCES.—(1) Relation from van Loon 2007; (2) Groenewegen et al. 2007; (3) Le Bertre 1997 ; (4) Relation from Le Bertre 1997; (5) Groenewegen et al. 2002; (6) Loup et al. 1993; (7) Bergeat & Chevallier 2005.

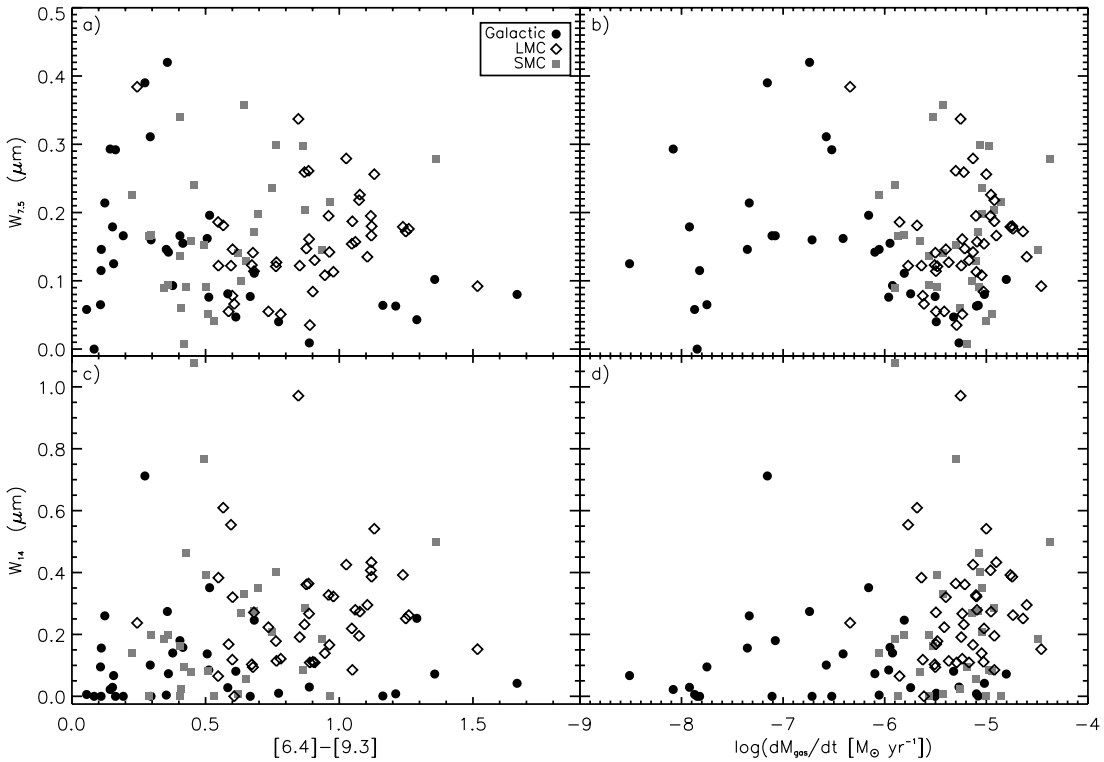

FIG. 7.—From left to right, the top panels plot the equivalent widths for the C_2H_2 *P*- and *R*-branches at 7.5 μm as a function of [6.4] – [9.3] color (dust mass-loss rate) and gas mass-loss rates, respectively. The bottom panels show the equivalent widths for C_2H_2 *P*- and *R*-branches at 14 μm as a function of [6.4] – [9.3] and gas mass-loss rates. [*See the electronic edition of the Journal for a color version of this figure.*]

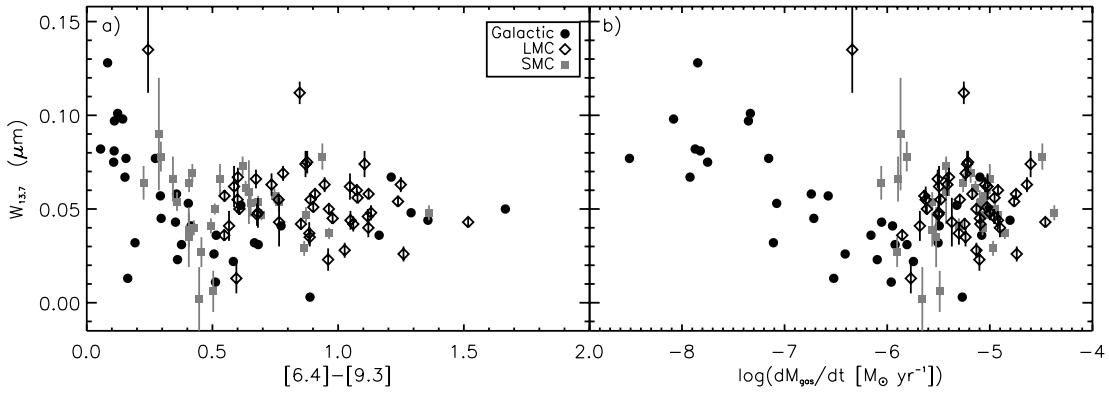

FIG. 8.—(*a*) Equivalent width for the 13.7 μm C_2H_2 *Q*-branch as a function of the [6.4] − [9.3] color (dust mass-loss rate). (*b*) C_2H_2 equivalent width for the 13.7 μm *Q*-branch as a function of the derived gas mass-loss rate. [*See the electronic edition of the Journal for a color version of this figure.*]

Although we observe the more obvious effects of dust dilution at lower optical depths and lower $\dot{M}$, we still support the conclusions of Matsuura et al. (2006) that the molecules exist throughout the envelope. Since the equivalent widths do not continue to decline at higher mass-loss rates where photospheric molecules would be veiled by the overlying dust, then the absorbing molecules most likely exist throughout the circumstellar envelope.

4.2. *Dust Emission*

4.2.1. SiC *Central Wavelength*

The central wavelength of the SiC feature (λ_{SiC}) has been used to infer dust properties and circumstellar geometry (Speck et al. 2005), but is very sensitive to the placement of the continuum. Despite the improved continuum determination, spectra with prominent acetylene bands at 14 μm continue to affect the central wavelength by removing emission from the SiC feature (Fig. 9*a*). Objects with larger λ_{SiC} tend to have little C_2H_2 absorption while objects with significant C_2H_2 absorption have λ_{SiC} occurring toward the blue. Zijlstra et al. (2006) and Lagadec et al. (2007) raise the possibility that since the C_2H_2 absorption overlaps the SiC emission, the red wing of the SiC feature is suppressed and causes the central wavelength to shift toward shorter wavelengths (see also Fig. 10*a*).

C_2H_2 suppression can explain the initially decreasing trend for Galactic stars when plotting [6.4] − [9.3] against λ_{SiC} reported by Sloan et al. (2006) and displayed in Figure 9*b*. Most of the blue Galactic objects have little C_2H_2 absorption; therefore, the SiC feature has not been altered on the long-wavelength side. At the same time, absorption at ∼10 μm lowers emission from the blue side of the SiC feature, as shown in Figure 10*b*. This has the opposite effect of the C_2H_2 absorption, causing λ_{SiC} to be artificially shifted to longer wavelengths as the temperature increases ([6.4] − [9.3] color decreases). Thus, for the bluest objects, we observe λ_{SiC} to be redder than the lab data.

For [6.4] − [9.3] $\gtrsim$ 0.4, Galactic carbon stars show increasing λ_{SiC} with increasing values of [6.4] − [9.3]. SMC stars appear to follow the same general trend as the Galactic sample over the observed color range, albeit a little less pronounced (Fig. 9*b*). However, the sample of SMC objects contains fewer stars overall and spans a much smaller color range. LMC stars, on the other hand, show a fairly consistent central wavelength between 11.1 and 11.2 μm for [6.4] − [9.3] = 0.5 to 1.5. These objects contain some of the most substantial 14 μm C_2H_2 bands, which dramatically affects the observed SiC central wavelength.

The different trends of the SiC central wavelength observed for the LMC, SMC, and Galactic samples at [6.4] − [9.3] $\gtrsim$ 0.4 can all be explained by a competition between self-absorption of the SiC feature and effects from C_2H_2 absorption. SiC self-absorption shifts the feature from 11.3 μm toward the red while the broad 14 μm C_2H_2 absorption band causes the SiC feature to shift toward the blue. Hence, objects containing little C_2H_2

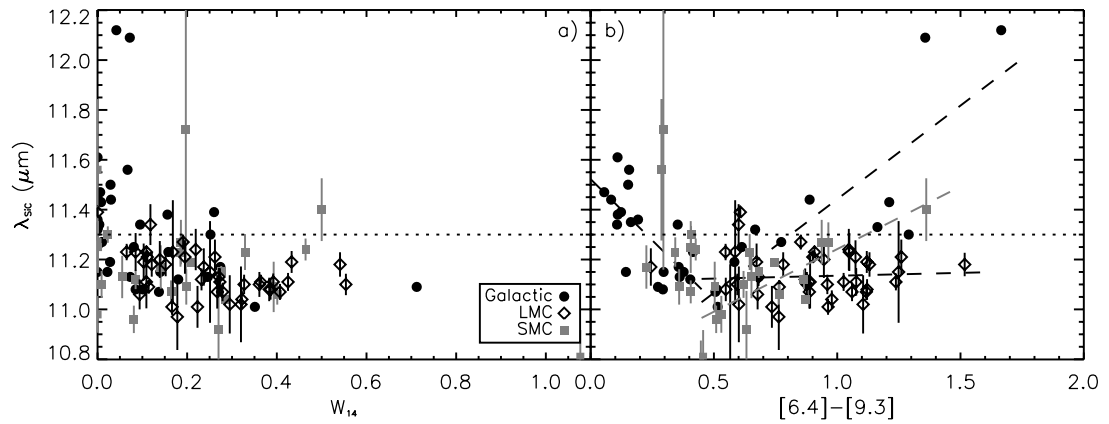

FIG. 9.—(*a*) Correlation between the 14 μm equivalent width and SiC central wavelength. Error bars for Galactic objects are smaller than symbols. Objects with increasingly large C_2H_2 band absorptions tend to have λ_{SiC} shifted further toward the blue while objects with redder λ_{SiC} have smaller C_2H_2 equivalent widths. (*b*) SiC apparent central wavelength as a function of the [6.4] − [9.3] color similar to Figs. 9 and 10 from Sloan et al. (2006). The dashed lines are linear fits to trends described in the text. The horizontal dotted line indicates the SiC central wavelength observed in laboratory data. [*See the electronic edition of the Journal for a color version of this figure.*]

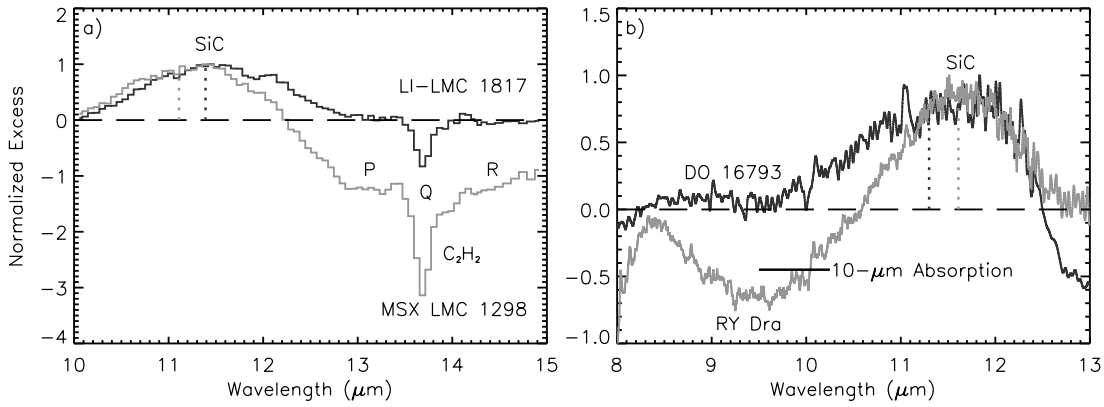

FIG. 10.—(*a*) Dark line shows the normalized continuum-subtracted spectrum of LI-LMC 1817. Overplotted in gray is the spectrum of MSX LMC 1298. C_2H_2 absorption including *P*-, *Q*-, and *R*-branches are labeled, as well as the SiC emission feature. The vertical dotted lines indicate the centroid of the SiC feature as it is affected by C_2H_2 absorption. (*b*) The spectrum of DO 16793 is plotted in black, while RY Dra is in gray. The 10 μm absorption and SiC emission features are labeled, and the vertical dashed lines show the shift of λ_{SiC} when affected by the absorption band.

absorption show a steeper slope with increasing optical depth (i.e., Galactic sample). Since the Magellanic Cloud samples contain significantly wider C_2H_2 bands, the slope of this trend decreases.

Two objects, AFGL 341 and IRAS 21489+5201, stand out with extremely red central wavelengths at about 12.1 μm. These particular objects are among the reddest sources, exhibit no apparent 10 μm absorption feature, and contain a relatively weak C_2H_2 absorption at 14 μm. Thus, self-absorption of the SiC feature most likely produces the considerable shifts in the central wavelength for these two objects.

While self-absorption of the SiC feature may have a considerable effect on trends of the Galactic sources, it is difficult to make a conclusive statements due to the molecular absorptions flanking the dust feature. We find only two objects in our entire sample that exhibit a shift in λ_{SiC} mainly due to SiC self-absorption. Therefore, one must be careful when making claims about the state of the SiC optical depth and self-absorption based purely on the position of its central wavelength, especially in the presence of strong molecular bands.

4.2.2. SiC *Feature Strength*

For a given $[6.4]-[9.3]$ color (which correlates with dust optical depth and $\dot{M}_{dust}$), the line-to-continuum ratio of the SiC emission feature appears largest for Galactic objects, but shows no appreciable difference between the LMC and SMC objects over their overlapping color range of $0.5 < [6.4]-[9.3] < 1.0$ (Fig. 11*a*). Plotting the SiC strength against the gas mass-loss rate provides a good indication of the observational bias inherent in the Magellanic Cloud samples (Fig. 11*b*). GRRV 38 and RAW 960 are the only two sources within the Magellanic Clouds with $\dot{M}_{gas} \leq 10^{-6}$ $M_\odot$ yr^{-1}, while about 20 Galactic objects span the range between 10^{-9} and 10^{-6} $M_\odot$ yr^{-1}.

While trends within the Magellanic Clouds are difficult to discern due to the large scatter of the SMC sources and small number of LMC sources with $[6.4]-[9.3] \lesssim 0.5$, the Galactic sources increase rapidly and peak at $[6.4]-[9.3] \sim 0.5$, matching the observations by Sloan et al. (2006). This same trend also transfers to Figure 11*b* with a general increase in SiC emission relative to carbon emission from low (10^{-9} $M_\odot$ yr^{-1}) to intermediate ($10^{-6.5}$ $M_\odot$ yr^{-1}) mass loss.

Moving toward redder colors and higher mass-loss rates, the SiC strength subsequently decreases. The starting point of this decline appears to depend on metallicity. This trend is most pronounced in the Galactic objects which initially increases, then plateaus, and finally decreases between 10^{-9} and $10^{-4.8}$ $M_\odot$ yr^{-1}. The same decreasing trends for the LMC and SMC samples occur at $\dot{M}_{gas} \sim 10^{-5.3}$ and $\dot{M}_{gas} \sim 10^{-5.0}$ $M_\odot$ yr^{-1}, respectively, and line up well with the Galactic objects.

The trend of decreasing SiC with increasing color could result from self-absorption within the feature due to an outer layer of cooler dust rather than a decrease in actual SiC grain emission (Speck et al. 2005) and may explain the observations of IRAS 04496−6958 (Speck et al. 2006). However, this trend also correlates with the onset of MgS emission and may be more closely linked to the dust condensation sequence (see §§ 4.2.3 and 5).

4.2.3. MgS *Feature Strength*

Every carbon star throughout the entire range of color temperatures presented here contains an apparent SiC dust feature; however, less than half of the entire sample show a MgS band. Only 6 out of 29 carbon stars in the SMC sample exhibit a MgS feature, 27 out of 44 in the LMC, and 14 out of 34 for Galactic sources.

Throughout the entire sample, there appears to be an overarching trend for redder objects to contain a stronger MgS emission relative to the continuum. All objects with a $[6.4]-[9.3]$ color greater than 0.9 (corresponding to a $T_{cont} \lesssim 500$ K) contain a significant MgS dust feature, while all objects with $[6.4]-[9.3] <$ 0.6 show no emission from MgS, with the exception of V Cyg, V CrB, and T Dra in the Milky Way. This is consistent with the condensation temperature of MgS (∼600–300 K), which is always lower than the SiC condensation temperature.

We also find that the MgS condensation temperature depends on pressure. Plotting the MgS strength in terms of the gas mass-loss rate reveals that the majority of objects with an MgS feature lie within a relatively small mass-loss range, albeit a bit offset in terms of metallicity. About half of the Galactic spectra containing an MgS feature have continuum dust temperatures greater than the condensation temperature. Hony & Bouwman (2004) have explained this phenomenon in terms of an optically thin detached dust shell due to time-variable mass loss. Such objects are identified by a blue spectrum, low mass-loss rate, and weak MgS feature.

Each metallicity environment appears to contain a sharp transition region where MgS emission is observed which occurs at different mass-loss rates and color temperatures (Fig. 11, *vertical dotted lines*). These offsets can be attributed to metallicity differences and can be used to constrain the conditions under which we would expect to observe MgS grain emission, assuming the MgS and amorphous carbon exist in the same volume (i.e., no detached dust shell).

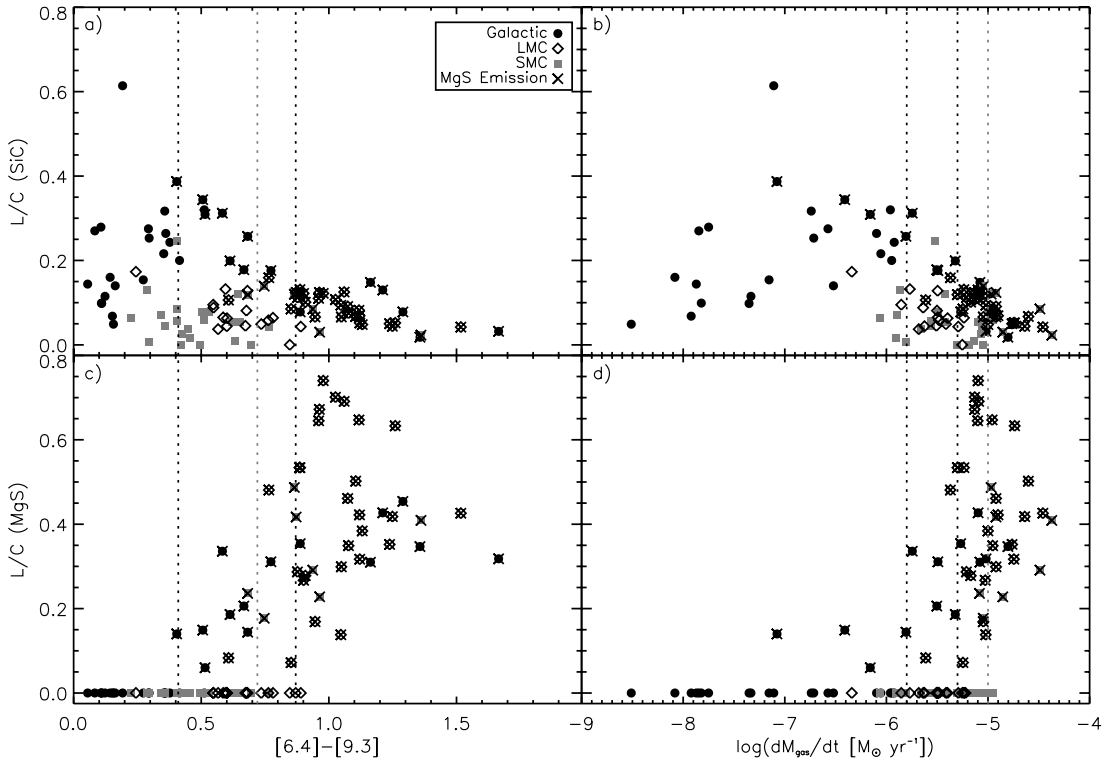

FIG. 11.—Plots of the SiC and MgS dust feature strengths with respect to the [6.4] − [9.3] color (dust mass-loss rate) and the gas mass-loss rate. Objects with a measurable MgS emission feature have been marked in the top two panels with black crosses. In general, redder sources have a weaker SiC emission and correlate with the presence of MgS. Dotted lines in all panels indicate the transition point in each metallicity system from objects without any MgS to objects with MgS emission. [*See the electronic edition of the Journal for a color version of this figure.*]

These transition points also correspond with the decrease in SiC emission discussed in § 4.2.2. Figures 11*a* and 11*b* show the correlation between SiC emission strength and the MgS feature with respect to the dust and gas mass-loss rates. Objects containing weak MgS features mainly occupy positions near the peaks of the SiC trend discussed above. As MgS intensity strengthens, SiC declines, suggesting that the MgS condenses in the form of a coating on top of the SiC grains, thus suppressing the SiC emission (see § 5).

5. DUST CONDENSATION SEQUENCE

In order to decipher the dust condensation sequence in carbon stars, we must first constrain various parameters in the envelope such as temperature, gas pressure (density), C/O ratio, and abundance (metallicity). For solar-metallicity stars, Lodders & Fegley (1995) give the condensation temperatures of C, SiC, and MgS for varying C/O ratio and pressure (Fig. 12*a*). At a given C/O ratio and pressure, Lodders (2006) shows that the condensation temperatures will decrease with decreasing metallicity; however, this effect is more pronounced for carbon than for SiC or MgS. Figures 12*b* and 12*c* plot the estimated shift in the condensation temperatures for metallicities corresponding to the LMC and SMC, respectively. We also compare the radial structure of a stellar model from Woitke (2006) to show the approximate regions and sequence of various dust condensates. Furthermore, Jørgensen et al. (1992) show that for a given mass, decreasing the effective temperature or the C/O ratio will generally shift this curve downward and to the left. A reduction in the metallicity similarly reduces the pressure at a given radius, but the temperature structure will remain fairly constant.

Observationally, prominent MgS does not appear until the mass-loss rates for Galactic, LMC, and SMC objects become greater than $10^{-5.8}$, $10^{-5.4}$, and $10^{-5.1}$ $M_\odot$ yr^{-1}, respectively (Fig. 11*d*). We therefore support the conclusions from Lodders (2006) that for a given temperature, decreasing the metallicity also leads to an increase in the critical density at which MgS condenses.

Figure 13 is a schematic of the trends we expect to see for three different dust condensation sequences to which this method is sensitive. These can be differentiated by analyzing the change in the SiC-to-C ratio with $\dot{M}_{\rm gas}$ and taking into account the formation of MgS (Fig. 11*b*):

Sequence I, C → SiC → MgS.—In general, carbon stars will start with a low C/O ratio and a low mass-loss rate. As the wind expands away from the star and the temperature decreases, carbon grains condense first. As the temperature further decreases, SiC will condense and coat the already existing carbon grains, raising the relative emission of SiC. Finally, as mass loss increases and the shell further expands and cools, MgS will condense last onto existing dust grains. In this scenario, one would expect no SiC emission for low $\dot{M}$, then a gradually increasing SiC feature for intermediate mass-loss rates. Higher $\dot{M}$ would be characterized by a decrease in the SiC strength due to MgS coating the SiC dust grains.

Sequence II, SiC → C → MgS.—In this case, SiC would condense first at low mass-loss rates and be characterized by a sharp increase in the SiC-to-C ratio. Carbon condenses next as mass loss progresses and the circumstellar envelope cools, reducing the SiC-to-C ratio. MgS forms last on the existing existing grains, further reducing the SiC strength.

Sequence III, SiC → (C, SiC) → MgS.—This scenario is characterized by an initially rapid increase of SiC emission. If the C/O ratio, metallicity, and density are such that SiC and C have comparable condensation temperatures, then we would observe a

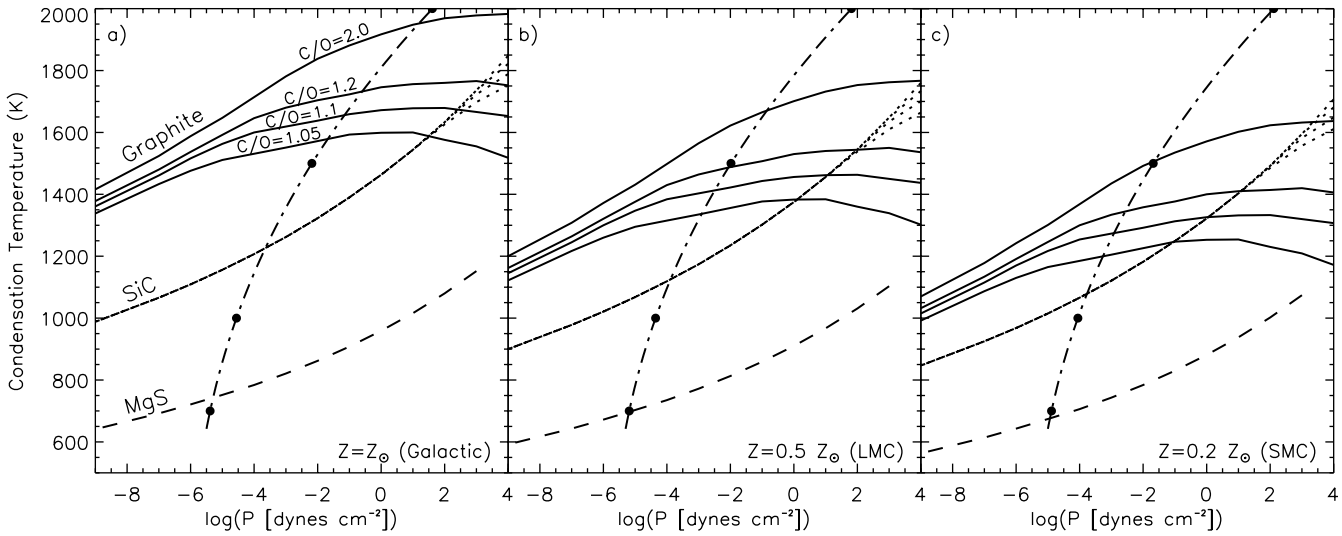

FIG. 12.—Condensation temperatures of carbon graphite, SiC, and MgS as a function of the total pressure and C/O ratio (1.05–2.0) based on Lodders & Fegley (1995). Data for the LMC and SMC are scaled from Lodders (2006). The dash-dotted line shows a model atmosphere for a carbon AGB star with the following parameters: $M_* = 1\ M_\odot$, $L_* = 10^4\ L_\odot$, $T_{\rm eff} = 2400$ K, and C/O = 1.7 (Woitke 2006). The filled circles correspond to a radius of $1.1R_*$, $1.5R_*$, $3R_*$, and $6R_*$ from top to bottom. The curves in panels *b* and *c* have been shifted to compensate for metallicity effects.

subsequent SiC-to-C ratio that is constant with $\dot{M}$ until MgS begins to condense. Afterward, the observed SiC strength would decline.

Lagadec et al. (2007) argue for a SiC → C condensation sequence for C stars in the Galaxy. Figures 11*a* and 11*b* show that the relative emission of SiC-to-C for Galactic objects increases at low mass-loss rates; but due to the large scatter and high uncertainties at low $\dot{M}_{\rm gas}$, we are unable to determine with absolute certainty whether the trend levels off or continues to increase until $10^{-6}\ M_\odot\ {\rm yr}^{-1}$. If it does indeed flatten at $\dot{M}_{\rm gas} \sim 10^{-7.3}\ M_\odot\ {\rm yr}^{-1}$, this would suggest a scenario where SiC forms initially; then, as the mass-loss rate increases, C and SiC condense simultaneously. However, based on the increasing trend in Figure 11*a*, as well as observational evidence of presolar grains indicating that Galactic carbon stars produce mainly uncoated SiC grains (Bernatowicz et al. 1987), it is more likely that the SiC-to-C ratio increases until $\dot{M}_{\rm gas} \sim 10^{-6}\ M_\odot\ {\rm yr}^{-1}$ supporting a C → SiC condensation sequence. The subsequent decline in SiC strength correlates with an increase in MgS emission indicating that MgS is condensing onto the SiC grain.

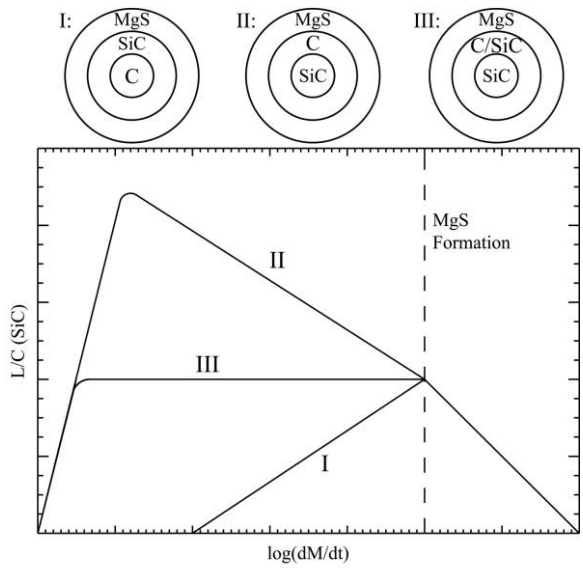

FIG. 13.—Expected SiC-to-C ratio against mass-loss rate for three separate grain condensation sequences (shown at the top). The dashed line indicates the onset of MgS grain condensation.

Due to the lack of objects with low mass-loss rates observed in the Magellanic Clouds, it is difficult to discern whether SiC or graphite grains form initially. However, the fact that we observe a relatively large scatter in the SiC-to-C ratio for objects without MgS emission (especially for the SMC sample) suggests near-simultaneous condensation of SiC and carbon, supporting a SiC → (C, SiC) sequence. Similarly, Lagadec et al. (2007) suggest that SiC and C form close together in the LMC, but that SiC forms last in the SMC stars. A low initial Si abundance may also contribute to the observed low SiC strength in these environments, particularly in the SMC. Finally, similar to the Galactic stars, a decline in SiC strength is observed as MgS increases for both the LMC and SMC objects.

Based on the positions of the model from Woitke (2006) in the three panels of Figure 12, stars with higher metallicities would more likely follow a C → SiC → MgS condensation sequence in an outflowing wind. Lowering the photospheric temperature and/or the C/O ratios would shift the model atmosphere curves down and to the right (Jørgensen et al. 1992). This would not affect the condensation sequence for Galactic carbon stars due to the initially large spread between the condensation zones for the different dust species; but it could potentially flip the C/SiC sequence shown for the Magellanic Clouds samples, especially for the SMC stars. However, the increased efficiency of carbon dredge-up leading to relatively higher C/O ratios at lower metallicities effectively reduces our ability to shift the LMC and SMC models. Thus, this supports the above suggestion that carbon stars in both Magellanic Clouds have SiC → (C, SiC) → MgS sequences.

6. CONCLUSIONS

We analyze a combined total of 107 carbon-rich AGB stars in the LMC, SMC, and Milky Way to investigate the effects of metallicity on dust and molecular species in these objects' circumstellar envelopes. Using modified blackbody fits, we isolated and

studied the spectral features throughout the 5–38 μm range including the *P*-, *Q*-, and *R*-branches of C_2H_2 absorption at 7.5, 13.7, and 14 μm; the 11.3 μm SiC emission feature; and the 30 μm MgS emission feature.

The modified blackbody fits deviate from the Manchester method used in SZL by providing a more robust method of determining the continua above and below the aforementioned spectral features. In particular, this work improves on the existing IRS studies from SZL by allowing us to isolate the *P*- and *R*-branches in the 14 μm C_2H_2 band. For a given gas mass-loss rate, we find that LMC and SMC objects have comparable C_2H_2 equivalent widths, contrary to the findings of SZL. However, in agreement with SZL, we also find that carbon stars within the LMC and SMC have much larger C_2H_2 equivalent widths than Galactic carbon stars for a given $\dot{M}_{\rm gas}$, which can be explained by a combination of more efficient carbon dredge-up and less dust dilution at lower metallicities.

For the 13.7 μm C_2H_2 *Q*-branch, we show that dust dilution plays a prominent role on the shape and strength of this feature at lower mass-loss rates. However, at higher $\dot{M}$, C_2H_2 absorption overcomes the effects of dust dilution due to increasing densities. Since veiling of the absorbing molecules by dust does not increase with the mass-loss rates, we confirm the previous results from Matsuura et al. (2006) and SZL that the 13.7 μm C_2H_2 absorption band must originate throughout the circumstellar dust shell. Conversely, the effects of dust veiling on the *P*- and *R*-branches become apparent at higher gas mass-loss rates ($\dot{M}_{\rm gas} \gtrsim 10^{-6.5}\ M_\odot\ {\rm yr}^{-1}$). This supports the idea that the optimal conditions for *P*- and *R*-branch transitions occur at depths below those favoring *Q*-branch transitions.

For objects with low to moderate mass-loss rates, we find that the molecular absorption band at 14 μm affects the position of $\lambda_{\rm SiC}$. The adjoining *P*-branch of strong acetylene absorption effectively reduces flux on the red side of the SiC feature causing $\lambda_{\rm SiC}$ to shift toward the blue. This effect occurs more prominently in the Magellanic Clouds because of the increased C_2H_2 abundance due to enhanced carbon dredge-up. Similarly, an unidentified absorption feature at around 10 μm shifts $\lambda_{\rm SiC}$ toward longer wavelengths for objects with $[6.4]-[9.3] \lesssim 0.2$. SiC self-absorption dominates the shift in $\lambda_{\rm SiC}$ for objects with large dust optical depths ($[6.4]-[9.3]$ color) and small C_2H_2 absorption at 14 μm. Differences in trends between Galactic, LMC, and SMC sources reflect the variation of C_2H_2 with metallicity for a given $[6.4]-[9.3]$ color.

Based on emission features of the SiC and MgS dust components with respect to the mass-loss rate, we have developed a method to determine the dust condensation history for a given metallicity system. We find evidence to support a C $\rightarrow$ SiC condensation sequence in Galactic objects. For C stars within the Magellanic Clouds, we suggest that a SiC $\rightarrow$ (C, SiC) sequence best fits the observed data. Formation and an increase of the MgS feature with $\dot{M}_{\rm gas}$ corresponds to a decrease in the SiC strength indicating that MgS inhibits the SiC emission by coating the SiC grains. The condensation of MgS in circumstellar atmosphere appears to be delayed until higher pressures for decreasing metallicities.

The precision of much of this analysis depends on our ability to accurately determine individual gas mass-loss rates. In this work, we make three major assumptions that lead to uncertainties when deriving $\dot{M}_{\rm gas}$: (1) the objects in each galaxy are comprised of the same metallicity; (2) the dust-to-gas ratio scales with metallicity; and (3) $\dot{M}_{\rm gas}$ can be derived from the dust-to-gas ratio and $\dot{M}_{\rm dust}$. Any of these assumptions may contribute to the large scatter observed in Figure 11*b* for the non-MgS-bearing objects in the Magellanic Clouds, as well as deviations from the analysis by SZL when comparing gas mass-loss rates. Therefore, we are anticipating more accurate determinations of the gas mass-loss rate from direct measurements of molecular species such as CO, particularly in the Magellanic Clouds. Differences between CO-determined $\dot{M}_{\rm gas}$ and those derived in this and previous works will further improve our understanding of dust formation efficiencies as a function of metallicity.

We thank Eric Lagadec and Albert Zijlstra for careful readings of the manuscript and providing us with valuable comments. This work is based on observations made with the *Spitzer Space Telescope*, which is operated by the Jet Propulsion Laboratory, California Institute of Technology, under NASA contract 1407. Support for this work was provided by NASA through contract number 1281150 issued by JPL/Caltech. We are grateful to the PIs Peter Wood and Michael Egan for making available the reduced data of their *Spitzer* observations (PIDs 3505 and 3277, respectively). We have made use of data products from the Two Micron All Sky Survey, which is a joint project of the University of Massachusetts and the Infrared Processing and Analysis Center at Caltech, funded by NASA and the National Science Foundation. This research has also made use of the SIMBAD and VizieR databases, operated at the Centre de Données astronomiques de Strasbourg, and the Infrared Science Archive at the Infrared Processing and Analysis Center, which is operated by JPL.

REFERENCES

Aoki, W., Tsuji, T., & Ohnaka, K. 1998, A&A, 340, 222
———. 1999, A&A, 350, 945
Bergeat, J., & Chevallier, L. 2005, A&A, 429, 235
Bernatowicz, T., Fraundorf, G., Ming, T., Anders, E., Wopenka, B., Zinner, E., & Fraundorf, P. 1987, Nature, 330, 728
Bernatowicz, T. J., Croat, T. K., & Daulton, T. L. 2006, Origin and Evolution of Carbonaceous Presolar Grains in Stellar Environments (Tucson: Univ. Arizona Press)
Bernatowicz, T. J., & Zinner, E., eds. 1997, Astrophysical Implications of the Laboratory Study of Presolar Materials (New York: AIP)
Bertelli, G., Bressan, A., Chiosi, C., Fagotto, F., & Nasi, E. 1994, A&AS, 106, 275
Blanco, V. M., Blanco, B. M., & McCarthy, M. F. 1980, ApJ, 242, 938
Cernicharo, J., Yamamura, I., González-Alfonso, E., de Jong, T., Heras, A., Escribano, R., & Ortigoso, J. 1999, ApJ, 526, L41
Clayton, D. D., & Nittler, L. R. 2004, in Origin and Evolution of the Elements, ed. A. McWilliam & M. Rauch (Cambridge: Cambridge Univ. Press), 297
Dray, L. M., Tout, C. A., Karakas, A. I., & Lattanzio, J. C. 2003, MNRAS, 338, 973
Egan, M. P., Van Dyk, S. D., & Price, S. D. 2001, AJ, 122, 1844
Fleischer, A. J., Gauger, A., & Sedlmayr, E. 1995, A&A, 297, 543
Forrest, W. J., Houck, J. R., & McCarthy, J. F. 1981, ApJ, 248, 195
Gilra, D. P. 1971, Nature, 229, 237
Goebel, J. H., Bregman, J. D., Witteborn, F. C., Taylor, B. J., & Willner, S. P. 1981, ApJ, 246, 455
Goebel, J. H., & Moseley, S. H. 1985, ApJ, 290, L35
Groenewegen, M. A. T., Sevenster, M., Spoon, H. W. W., & Pérez, I. 2002, A&A, 390, 511
Groenewegen, M. A. T., et al. 2007, MNRAS, 376, 313
Habing, H. J. 1996, Astron. Astrophys. Rev., 7, 97
Herwig, F., Freytag, B., Fuchs, T., Hansen, J. P., Hueckstaedt, R. M., Porter, D. H., Timmes, F. X., & Woodward, P. R. 2007, in ASP Conf. Ser. 378, Why Galaxies Care About AGB Stars: Their Importance as Actors and Probes, ed. F. Kerschbaum, C. Charbonnel, & R. F. Wing (San Francisco: ASP), 43
Höfner, S., Feuchtinger, M. U., & Dorfi, E. A. 1995, A&A, 297, 815
Hony, S., & Bouwman, J. 2004, A&A, 413, 981
Hony, S., Waters, L. B. F. M., & Tielens, A. G. G. M. 2002, A&A, 390, 533
Houck, J. R., et al. 2004, ApJS, 154, 18

Hoyle, F., & Wickramasinghe, N. C. 1962, MNRAS, 124, 417
Jørgensen, U. G., Hron, J., & Loidl, R. 2000, A&A, 356, 253
Jørgensen, U. G., Johnson, H. R., & Nordlund, A. 1992, A&A, 261, 263
Lagadec, E., et al. 2007, MNRAS, 376, 1270
Lattanzio, J. C., Frost, C. A., Cannon, R. C., & Wood, P. R. 2000, in IAU Symp. 177, The Carbon Star Phenomenon, ed. R. F. Wing (Dordrecht: Kluwer), 449
Le Bertre, T. 1997, A&A, 324, 1059
Lodders, K. 2006, Pre-Solar Grains as Astrophysical Tools, 26th meeting of the IAU, Joint Discussion 11, 21 August 2006, Prague, Czech Republic, JD11, #6, 11
Lodders, K., & Fegley, B., Jr. 1995, Meteoritics, 30, 661
Loup, C., Forveille, T., Omont, A., & Paul, J. F. 1993, A&AS, 99, 291
Maeder, A. 1992, A&A, 264, 105
Martin, P. G., & Rogers, C. 1987, ApJ, 322, 374
Matsuura, M., Zijlstra, A. A., van Loon, J. T., Yamamura, I., Markwick, A. J., Woods, P. M., & Waters, L. B. F. M. 2002, ApJ, 580, L133
Matsuura, M., et al. 2005, A&A, 434, 691
———. 2006, MNRAS, 371, 415
Messenger, S., Keller, L. P., & Lauretta, D. S. 2005, Science, 309, 737
Nittler, L. R. 2003, Earth Planet. Sci. Lett., 209, 259
Olson, B. I., & Richer, H. B. 1975, ApJ, 200, 88
Pols, O. R., Tout, C. A., Lattanzio, J. C., & Karakas, A. I. 2001, in ASP Conf. Ser. 229, Evolution of Binary and Multiple Star Systems, ed. P. Podsiadlowski et al. (San Francisco: ASP), 31
Renzini, A., & Voli, M. 1981, A&A, 94, 175
Russell, S. C., & Bessell, M. S. 1989, ApJS, 70, 865
Salpeter, E. E. 1974, ApJ, 193, 585
Schwarzschild, M., & Härm, R. 1965, ApJ, 142, 855
Skrutskie, M. F., et al. 2006, AJ, 131, 1163
Sloan, G. C., Kraemer, K. E., Matsuura, M., Wood, P. R., Price, S. D., & Egan, M. P. 2006, ApJ, 645, 1118
Sloan, G. C., Kraemer, K. E., Price, S. D., & Shipman, R. F. 2003, ApJS, 147, 379
Speck, A. K., Cami, J., Markwick-Kemper, C., Leisenring, J., Szczerba, R., Dijkstra, C., Van Dyk, S., & Meixner, M. 2006, ApJ, 650, 892
Speck, A. K., Thompson, G. D., & Hofmeister, A. M. 2005, ApJ, 634, 426
Straniero, O., Chieffi, A., Limongi, M., Busso, M., Gallino, R., & Arlandini, C. 1997, ApJ, 478, 332
Treffers, R., & Cohen, M. 1974, ApJ, 188, 545
van Loon, J. T. 2000, A&A, 354, 125
———. 2007, in ASP Conf. Ser. 378, Why Galaxies Care About AGB Stars: Their Importance as Actors and Probes, ed. F. Kerschbaum, C. Charbonnel, & R. F. Wing (San Francisco: ASP), 227
van Loon, J. T., Marshall, J. R., Cohen, M., Matsuura, M., Wood, P. R., Yamamura, I., & Zijlstra, A. A. 2006, A&A, 447, 971
Vassiliadis, E., & Wood, P. R. 1993, ApJ, 413, 641
Weidemann, V. 1987, A&A, 188, 74
Werner, M. W., et al. 2004, ApJS, 154, 1
Whitelock, P. A., Feast, M. W., Marang, F., & Overbeek, M. D. 1997, MNRAS, 288, 512
Woitke, P. 2006, A&A, 452, 537
Zijlstra, A. A., Loup, C., Waters, L. B. F. M., Whitelock, P. A., van Loon, J. T., & Guglielmo, F. 1996, MNRAS, 279, 32
Zijlstra, A. A., et al. 2006, MNRAS, 370, 1961
Zinner, E., Nittler, L. R., Gallino, R., Karakas, A. I., Lugaro, M., Straniero, O., & Lattanzio, J. C. 2006, ApJ, 650, 350